The Pennsylvania State University

The Graduate School

Department of Aerospace Engineering

COMPUTATIONAL PREDICTION OF A LARGE-SCALE HP TURBINE FLOW AGAINST MEASURED AERODYNAMIC DATA

A Thesis in

Aerospace Engineering

by

Mitansh Sharad Doshi

Submitted in Partial Fulfillment

of the Requirements

for the Degree of

Master of Science

December 2018

The thesis of Mitansh Sharad Doshi was reviewed and approved* by the following:

Cengiz Camci
Professor of Aerospace Engineering
Thesis Advisor

Dennis McLaughlin
Professor Emeritus of Aerospace Engineering

Amy R. Pritchett
Professor and Head of the Department of Aerospace Engineering

*Signatures are on file in the Graduate School

ABSTRACT

This thesis presents a Reynolds-averaged Navier Stokes (RANS) equations-based computational validation of the Axial Flow Turbine Research Facility (AFTRF). The research turbine design was based on NASA's E3 "Energy Efficient Engine" concept with 23 stationary nozzle guide vanes and a 29 blade high pressure (HP) turbine rotor. This large-scale and low-speed turbomachinery research facility provides high-resolution aerodynamic measurements from the turbine stage for the assessment of computational simulations. The finite volume-based general purpose fluid dynamics solver, Star CCM+, coupled with the k-ω SST turbulence model and the "Gamma transition" flow model were used. Various performance parameters were measured, including velocity profiles, nozzle/blade airfoil static pressure coefficients, and total pressure. The previously measured experimental data sets and boundary conditions from the AFTRF were used in a computational validation. NGV (Nozzle Guide Vanes) and rotor validations were performed and total-to-total efficiency was discussed.

The present computational effort uses a "mixing plane" based stationary to rotating interface for stage calculations. A grid dependency assessment has been performed both on NGV and rotor flows. The computational results obtained at NGV-intraspace and rotor exit are compared to five-hole-probe based experimental data. The stage exit data from a Kiel probe are also compared to the current simulations. The current study concludes that the present computational model effectively predicts AFTRF aerodynamic flow features with good spatial resolution. An attempt is also made to compare the total-to-total efficiency distribution in the spanwise direction. The study concludes that this computational approach can be effectively used in turbine secondary flow reduction, tip leakage flow mitigation, unsteady flow computations and finally energy efficiency improvements.

TABLE OF CONTENTS

LIST OF FIGURES

LIST OF TABLES

Nomenclature

c = midspan axial chord length of nozzle guide vane, m

C_P = pressure coefficient ;($P_1 - P_2$)/ (0.5ρU_m^2)

$C_p{}'$= static pressure coefficient; ($P_2 - P_{3avg}$)/ (0.5$\rho_2 W_{x2,avg}^2$)

C_{pt} (Rotor) = total pressure coefficient; ($P_{03} - P_{01}$)/ (0.5ρV_1^2)

C_{Pt} = total pressure coefficient; ($P_{02} - P_{01}$)/ (0.5ρU_m^2)

k = turbulent kinetic energy; $\frac{m^2}{s^2}$

P = Static Pressure, Pa

P_0= total pressure, Pa

T_0 = total temperature, K

U_m = blade speed at mean radius, m/s

V = velocity magnitude, m/s

V_x = axial velocity component, m/s

V_r = radial velocity component, m/s

V_θ = tangential velocity component, m/s

W = total relative velocity, m/s

x = axial distance from nozzle guide vane leading edge, m

y^+= non-dimensional wall coordinate

ω = vorticity

ε = dissipation rate

Subscript

1-Nozzle guide vane Inlet, One chord upstream of nozzle guide vane leading edge

2- Nozzle guide vane exit plane, x/c=1.025 from midspan trailing edge

3- Rotor Exit, x/c=1.5 downstream of the rotor trailing edge near casing)

Abbreviation

AFTRF- Axial Flow Turbine Research Facility

CFD- Computational Fluid Dynamics

NGV- Nozzle Guide Vanes

RANS- Reynolds Averaged Navier Stokes

SST- Shear Stress transport

TKE- Turbulent Kinetic Energy

HP- High Pressure

LP- Low Pressure

ACKNOWLEDGEMENTS

Woohoo! Finally I am writing this section to thank everyone who made this thesis possible. Caution, this section might be longer than it is supposed to be, this is just because I am feeling very thankful than normal ☺ . But do read this section even if you do not read my thesis, this section will tell you something interesting about the incredible people I met here at Penn State and in India. Please play the song "Take me home, Country Roads" by John Denver as you begin reading the rest of the acknowledgement.

First and Foremost, Thank you Dr.Cengiz Camci for giving me the opportunity to work under your guidance. I would always remember the value of patience and virtue that you taught me. Your kindness and humble nature have been great sources of motivation to finish this thesis. I appreciate your support for my academic and research growth. You are hands down the coolest professor I have ever met. Thanks for taking me on as your student even though you could have had many other students for the same position.

Richard Auhl and Ann Gael, I do not think so one paragraph would be enough to thank you guys. But here it goes, Professor Rick you are like Hagrid to this department. I will be forever in your debt for the kindness you have shown me. I still remember running behind you to get the first wage payroll job here in the department and you finally said yes. Who knew that it would be a great start to an awesome friendship! Since the day one you have taught me to smile no matter what and help as many people as you can. Ann thanks for always making us welcomed. You are awesome ☺

Dr. Dennis McLaughlin, those one minute conversations outside your office or somewhere in Hammond are something that I will always cherish. Thank you for being so positive and cheerful. (PS- I hope you enjoyed the hockey game on "Saturday")

I would like to thank EVERYONE from the aerospace department, you all are the best. Aerospace department is just like Hogwarts, Help is always given here to those who ask for it. Thank you for giving me the financial support through teaching assistantships to finish my Master's studies. Having that positive and open environment in the department has helped me a lot. Special shout out to Lindsay Moist (Former Graduate staff Assistant) and Maria Beaty (Current Graduate staff Assistant) for helping me with my silliest doubts.

I would like to Thank Aravinth Sadagopan for his assistance during the initial stage of my research. You have been a big help to set up the model from scratch. This thesis would not have been possible without your kind help. I appreciate you my friend. "All the wonders you seek are within yourself."

I would like to thank Amrat and Veerandra for their constant support throughout my research. Thanks Veerandra for always making annoying sounds while talking to me and ALWAYS answering my question with a question. You have taught me "What is pressure?" Amrat, thanks for coming to Penn state for your master's I am glad I got to spend a few more years with you after undergraduate degree. It has been a blessing to be

your friend and to have you in my life. Stay here for PhD too please? Gohar, thank you for your cheerful disposition and your cool way of saying things (I promise all of us would go to IP soon)

Thank you, Amit for your positivity and your laughter. I know you wouldn't care about this acknowledgement even though you have EQ higher than mine. Stay happy always and for love of god, start reading between the lines.

Ambarish the singer, thank you for inviting me to your concerts. Your singing always brought back my beautiful childhood memories, please keep inviting me for future shows. Vidhi, Niyati, Yash, Bhavya and Trusha skype call every once in a while would make me feel like I have not left India at all. Thank you all for being the most understanding group of friends I could ever ask for. You guys are my safe haven, more than 18 years we all have been together. I may not attend the skype calls at times but remember all the weird conversations are STILL fresh inside my head. Too glad we all are growing up together.

Benjamin Enders aka BATMAN, thanks for scaring me SO many times and recommending me good books. Your IT assistance has been always helpful. One thing I learnt from you is restarting any electronic item surprisingly fixes itself. Captain Kirk thanks for the compressed air can in your lab which has been a great stress reliever. Above everything else, thanks to both for your help in Star CCM+. Mr.Mark your help has been indispensable with Star CCM+ too.

Special thanks to Dr. Kaan Yildiz and Yeliz, I miss you guys a lot. Come and visit state college soon. ☺ We all could go for bowling soon. Kaan thanks for being there for me. Our journey started as TA colleagues and we surprisingly stayed friends even after that. This thesis would not have been possible without the chocolate frog card from Universal studios.

Adish and Nikita thank you for your coming into my life. Adish thanks for CONSTANT and UNWAVERING support. "Just saying thank you will never repay your kindness"

Special thanks to FiGE, I got to meet so many incredible people from all around the world. Gloria, Susanna, Sara, Zeynep, Yagmur, Han, Fabio etc. (there are more than 10).

Ameya and Mohit thanks for being awesome roommate and always being at home whenever I forgot my keys to home. Thanks for the emotional support you guys gave me. You guys along with Amrat made D-223 home. ☺ Thank you Sarthak, I will be graduating in December (COLD RUTHLESS PA WINTER) just like you did a year ago.

Thanks Kanika for your visiting me during spring semester.It was pleasure to have you visit me from India. I really enjoyed our reunion. Do plan the next trip soon. "Sometimes it takes an overwhelming breakdown to have an undeniable breakthrough"

Akshay(ASA) thank you for frequently doing the video calls without looking at the time. You have encouraged me a lot. Thanks Rupali for making him even a better person. Cannot wait to attend your wedding.

Aditi, Kaushal and Devashri thanks for always bringing the funny memories of VJTI. Even though we skyped rarely I thoroughly enjoyed every minute of it. Let's meet up soon in NYC!

Thanks to my lovely family. Bindu Doshi, Sharad Doshi, Yesha and Trusha. You guys have sacrificed everything for me and I would forever be grateful to you guys. Your emotional and financial support made this thesis. Bindu Doshi and Sharad Doshi talking to you both every day gave me an encouragement and kept me happy throughout the day. (If you are a student or a person reading this please go and call your parents right away). Yesha and Trusha thanks for talking to me for shorter period of time whenever I had work or something else. I know you guys would shower your "love" on me once I come to pick you up at the airport in December 2018. I cannot wait for you all to come here. ☺ I would also like to thank Shah, Mehta, Gandhi, Doshi, and Kansara family.

Last but not the least I would like to thank A-11, the best section I ever taught in 305W. Christian, Tyler, Matthew, John and Brenden. I do not know if I will ever get another A-11(probably not :P), but I am grateful I got to be your TA for one complete semester. And how could I forget the cake and the pizza? Thanks for making the lab fun.

Thank you for reading this LONG acknowledgment section. Hope you were smiling in-between. Now you are welcome to take the technical journey of this thesis by reading the remaining chapters or you can just read the Abstract and Conclusion and tell your supervisor or your friend this thesis ROCKS!!

Chapter 1 **Introduction**

1.1 Thesis Scope

Objective of this thesis is to computationally validate the Axial Flow Turbine Research Facility (AFTRF) available at Penn state University Heat Transfer and Turbomachinery lab. NGV (Nozzle Guide Vane) validation has been performed in the past for the same experimental facility however, there has not been detailed study of rotor validation. This thesis focuses on validating both the NGV and the rotor by comparing computational exit velocities profile, static pressure coefficient distribution, static pressure etc. against experimental data.

After performing the turbine stage (NGV and Rotor) validation, stage efficiency is also computed against the experimental data. A case study has been performed to show the effect of temperature on the stage efficiency plot.

Before starting the validation, it is a good practice to know what is a turbine and the possible losses which occur in a turbine. Section 1.2 and 1.3 deal with Background and typical losses in the turbine.

1.2 Background

A gas turbine is an important tool of turbomachinery which can be used for power generation, aviation or any other industry related purpose. Typical schematic of a gas turbine engine is shown in Figure 1-1. A gas turbine engine has the following components, Compressor, Combustor, Turbine, and Exhaust. Usually air comes from the intake and gets compressed in a compressor followed by the fuel injection in the combustion chamber and expansion in the turbine before leaving from exhaust. In this thesis, the focus is the axial flow turbine.

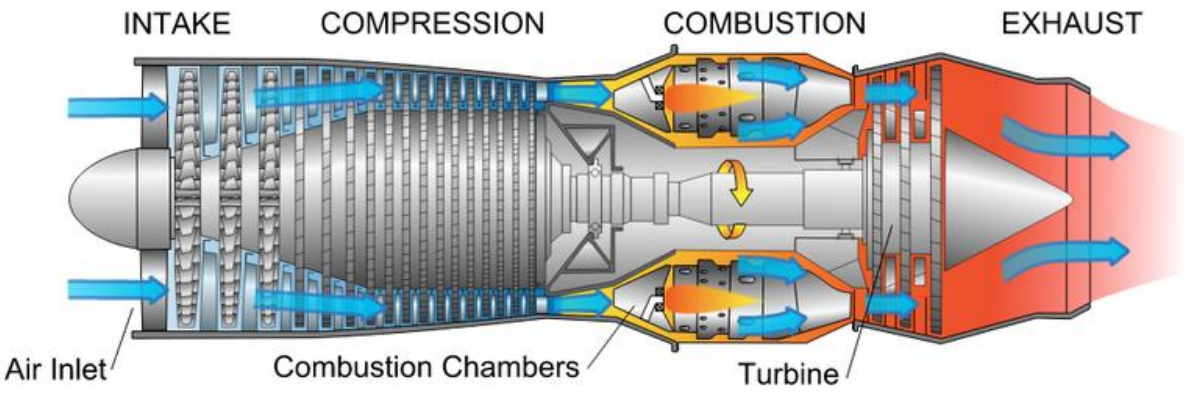

Figure 1-1 Axial flow gas turbine engine components [1]

Figure 1-2 shows the schematic of a multi-stage turbine. There are different components in a turbine. The stator or NGV is a stationary component in a turbine which is used to give the direction to the incoming flow. A rotor is a rotating part of the turbine which rotates at a certain RPM by extracting energy from the incoming flow. A single stage turbine has one stator and one rotor while multi-stage turbine as shown in Figure 1-3 has series of stator and rotors one after the other. Figure 1-2 and Figure 1-3 show a gap between the tip of the rotor and the casing; this gap is known as tip clearance, which is given by equation 1.1,

Tip clearance %= $\frac{t}{h}$ (1.1)

More details about the tip clearance calculations are shown in the Figure A-5

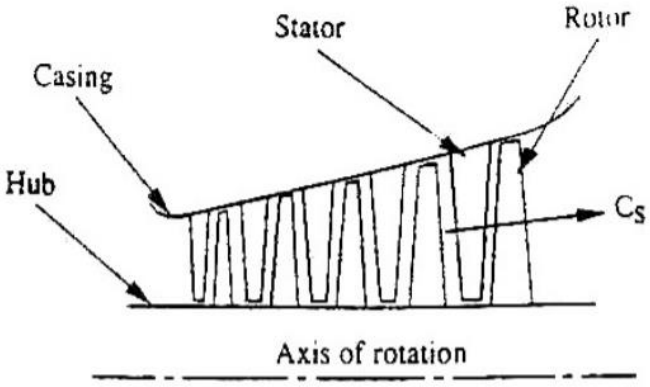

Figure 1-2 Component of a multi-stage turbine [2]

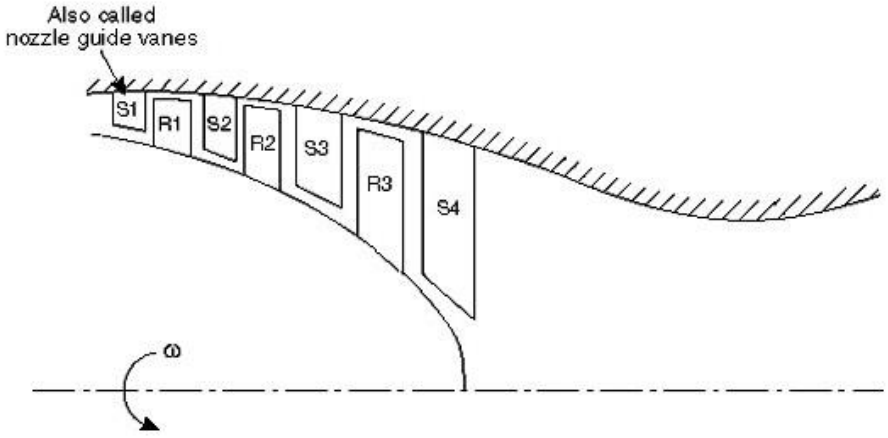

Figure 1-3 Component of a multi-stage turbine [2]

1.3 Losses in Turbine

Since the flow field in a turbine is complex and highly three dimensional, many studies have attempted to understand these flows [3], [4], [5], [6]. Computational Fluid Dynamics (CFD) has been a good tool to visualize the flow characteristics [5]. Even though turbines are usually able to achieve the efficiency of 92%, efforts have been made to increase the efficiency above 92%. Major sources of loss in a turbine efficiency are endwall flows and tip leakage flows. Sieverding [3] explains the details about the secondary vortex flow and experimental capabilities until 1985 whereas Langston [4] summarizes the recent capabilities about predicting the secondary flows until 2001 and states that still there has not been an accurate turbulence model to predict the endwall loss.

1.3.1 Secondary Flows

Secondary flows in a turbine includes Hub and casing endwall vortices, Horseshoe vortex, Counter Vortex, and Passage vortex. Viscous losses(endwall boundary layers of hub and casing surfaces, airfoil profile losses, wake losses) are responsible for 25% of the turbine stage loss. The remaining 75% of the turbine stage losses are associated with the blade (rotor). Most significant contributor to this major rotor loss is due to tip clearances, which accounts for one-third of the total stage loss [5]. Typical vortical structures around the turbine blade are shown in Figure 1-4

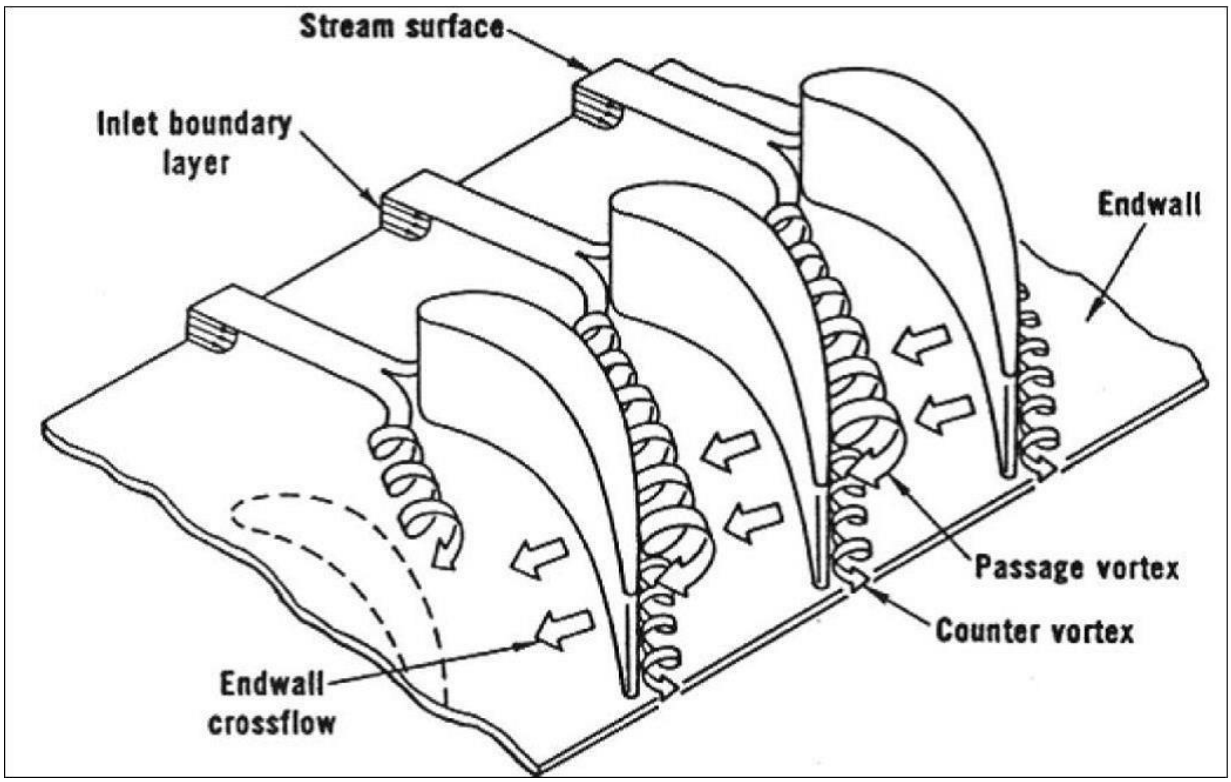

Figure 1-4 Three dimensional vortex structure around the blade surface [4]

Inlet boundary layer as shown in Figure 1-4, separates at a saddle point (location on the endwall where the zero degree incidence line meets the separation line) and forms horseshoe vortex. That vortex is further divided into two parts, pressure-side leg horseshoe vortex, and suction-side leg horseshoe vortex. The main driving force of the horseshoe vortex is pressure gradient along the blade surface, due to this pressure-side leg horseshoe vortex tries to move away from the surface and goes to the suction side of the next blade merging with the suction-side leg horseshoe vortex of the new blade (as shown in Figure 1-5). This leads to the generation of Passage vortex as shown in Figure 1-4

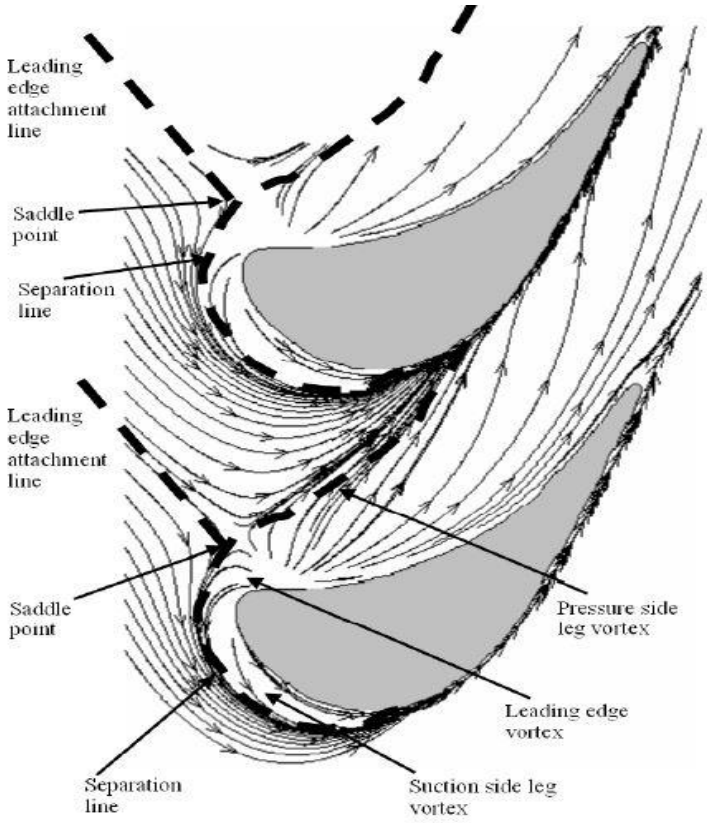

Figure 1-5 Streamlines representing the horseshoe vortex structure

Furthermore, at the leading edge, there is leading edge corner vortex (Pressure side and Suction side). Secondary flow model given by Goldstein and Spores [6] explains the formation of leading edge corner vortex, suction side, and pressure side corner vortices. As shown in Figure 1-6 is the model of secondary flow with corner vortices. Horseshoe vortex leads to the generation of leading edge corner vortex (Vortex 6-7), these corner vortices have the opposite direction of rotation as compared to the pressure and suction side leg horseshoe vortices. Note that the suction-side leg horseshoe vortex moves along the blade surface, away from the endwall due to lower pressure across the blade surface.

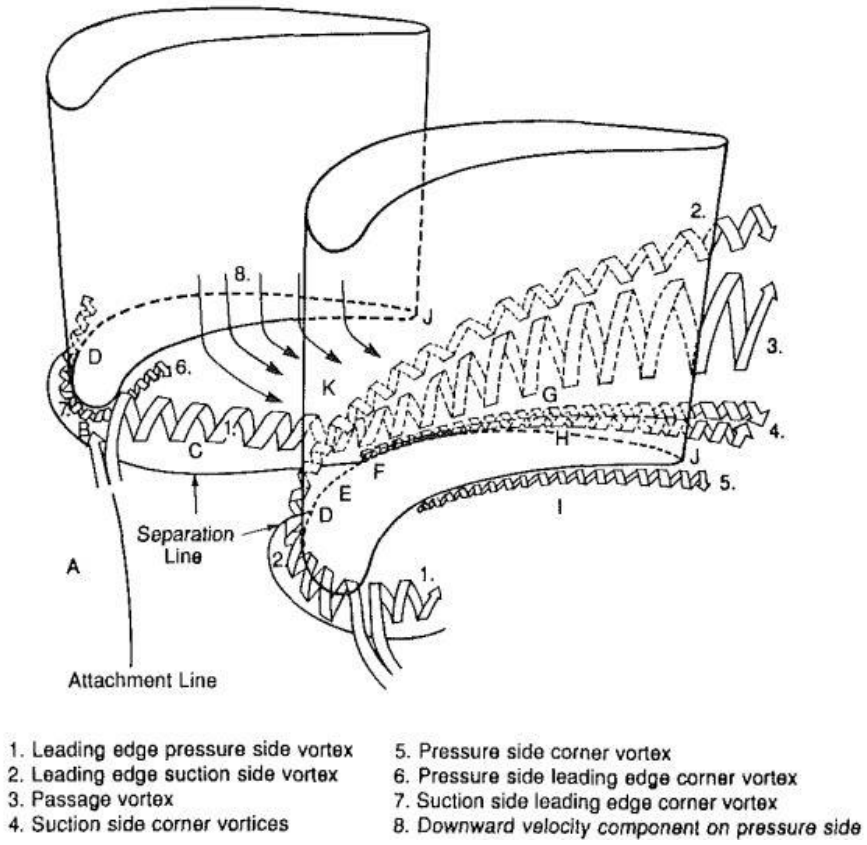

Figure 1-6 Secondary flow model of Goldstein and Spores [6]

Some secondary models like Sharma and Butler [7] have also shown that the suction-side leg horseshoe vortex wraps itself around the passage vortex. Vortex 4 is the pair of vortices which was observed by Sonada [8], according to Sonada this vortex pair is generated due to the interaction of suction side horseshoe vortex with the suction surface. Understanding these different vortex structures is critical because these vortex structures are responsible for the loss of lift and aerodynamic loss. Figure 1-7 shows the static pressure distribution on the pressure side and suction side surface at different span locations. Effect of passage vortex formed on the hub wall can be seen on the span location

(2.3%, 12.5% and 25.0% of span). Midspan (50% span) of the suction surface is not much affected by the three dimensional secondary flows. Overall, secondary flows try to decrease the area between the suction and pressure side which can be clearly seen for the lower span locations (2.3% span and 12.5% span). This decrease in the lift is the direct measure of loss in the work output.

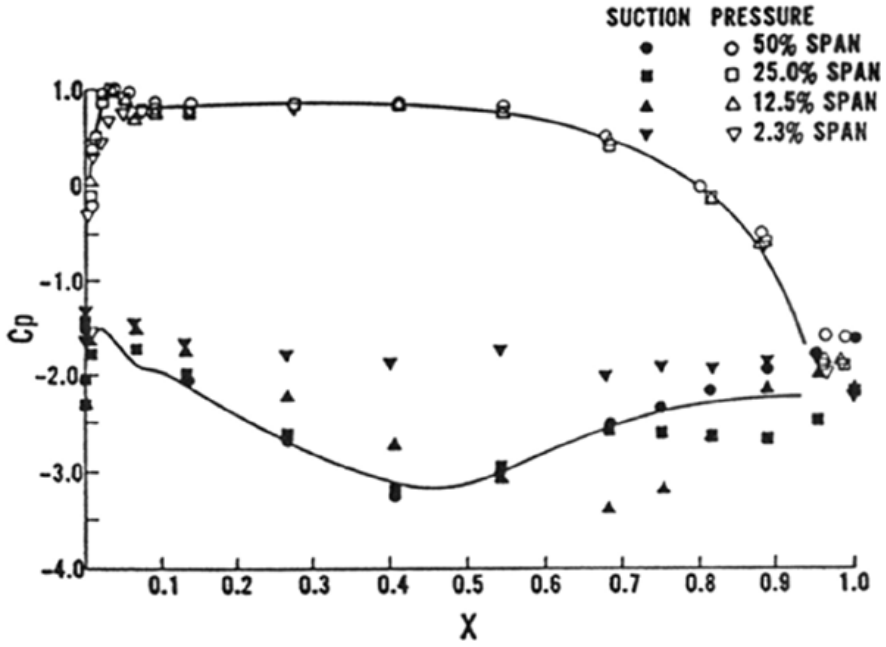

Figure 1-7 Static pressure distribution on the airfoil surface at different span locations [4]

Secondary flow structures in the blade are much stronger than the one in NGV, because of the high turning of the flow along the blade surface and the rotational effect.

1.3.2 Tip leakage vortex

Due to the pressure differences between the suction side and pressure side, flow exits the suction side with a high velocity at an oblique angle relative to the passage flow and interacts with the incoming passage flow which causes the leakage vortex to roll up into a vortical structure.

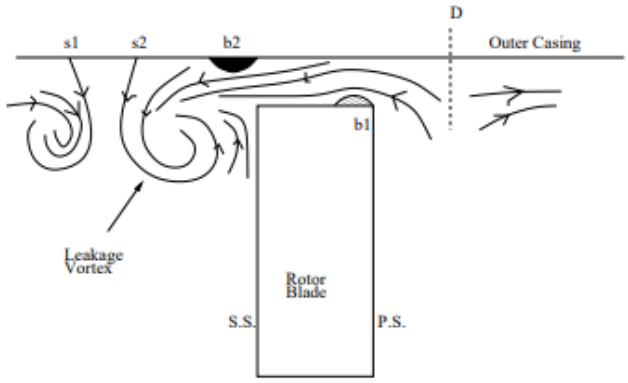

Figure 1-8 Schematic of leakage flow field in a linear cascade [9]

Figure 1-8 indicates the flow moving from the pressure side (P.S) to the suction side (S.S) through the tip gap with the stationary casing. While the flow goes from P.S to S.S the separation bubble b1 forms at the corner and it creates the vena contracta region which accelerates the flow. At times there is another circulation region b2 which is created as the tip leakage vortex moves further in the suction side. In actual turbine tip leakage flow may be more complicated than as shown in Figure 1-8 due to the rotational effect of the blade and shearing effect of the outer casing. Tip passage vortex is generated due to the blockage created from the tip leakage vortex. Interaction of tip passage vortex with tip leakage vortex has been a good topic of discussion in turbomachinery field. B.Lakshminarayana [10] mentioned that more research is still needed in the area of tip

leakage and secondary flow interactions for further improvements in axial turbine aero-thermal performance.

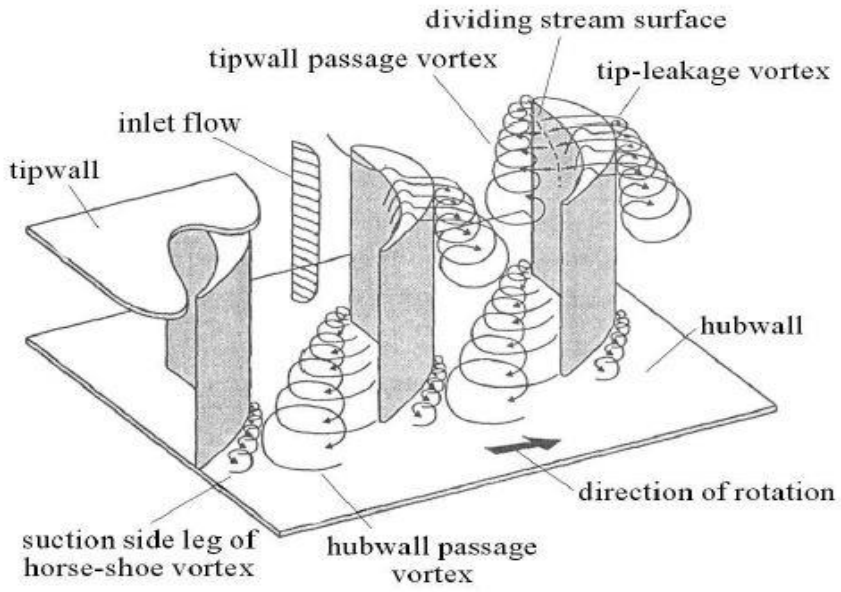

Figure 1-9 Tip leakage and other secondary flows [11]

Langston [4] did not consider the effect of tip clearance on secondary flows, as seen in Figure 1-9. Due to the clearance gap between the blade and the casing wall (tip wall), tip leakage flow forms. Because of the gap, there is no saddle point, hence, the horseshoe vortex also does not form. Formation of tip leakage creates blockage for the crossflow, and thus, the flow separates from the end wall and a passage vortex is created. The rotation of the tip leakage vortex and the passage vortex are opposite.

Capturing these losses (secondary flows and the tip leakage vortex) is critical in order to understand the flow physics inside a turbine stage. For this reason, and due to experimental limitations, developing a computational model that can predict these flows is essential.

1.4 Thesis organization

The current experimental facility (AFTRF) and the data collected therein are described in Chapter 2. An overview of the facility, including the number of NGVs and rotor blades, dimensions, and flow conditions are discussed. Measuring plane locations for the NGV and the rotor, along with the static pressure port locations for the rotor blade are also detailed. Sensors, data uncertainty, and boundary conditions are mentioned in this chapter.

The computational model, including the mesh and solid geometry are shown in Chapter 3. Different turbulence models, such as k□□□ k-□□ and Spalart-Allmaras are discussed in this chapter. Mesh/grid dependency studies were conducted on the rotor and the NGV to compute the final required grid cell size.

Chapter 4 describes the NGV and rotor validation. The NGV validation compared the simulation's total pressure coefficients, velocity components (axial, radial, and tangential), and static pressure distribution against the experimental data. For the rotor validation, total pressure coefficient and the velocity components were used.

Chapter 5 computes the total-to-total efficiency for a turbine stage. Turbine stage total pressure ratio and total temperature ratio are discussed. For the AFTRF (low pressure), the stage total temperature ratio has a significant effect on the total-to-total efficiency plot. A case study of a low pressure (LP) turbine and a high pressure (HP) turbine are presented. The stage total temperature ratio only had a significant contribution to the total-to-total efficiency of the LP turbine, and not the HP turbine.

Conclusions from the current research, as well as suggestions for future research, are summarized in Chapter 6.

Chapter 2 **Experimental Facility and Data Measurement**

Introduction to AFTRF is given in this chapter. It gives an overview about the facility and current data measurement techniques which were used to gather the experimental data. Experimental boundary conditions are also discussed which will be used for the computational model. Experimental data uncertainty is discussed at the end of the chapter associated with the sensors/probe.

The AFTRF is located in the Pennsylvania State University Heat Transfer and Turbomachinery Lab. It is a high pressure (HP), open loop, low speed, single stage, cold flow turbine facility, which was built to study three dimensional passage flows. The apparatus is 91.66 cm in diameter with a hub-to-tip ratio of 0.73. There are 23 NGVs and 29 rotor blades followed by outlet guide vanes (OGV). A schematic of the AFTRF facility is shown in Figure 2-1.

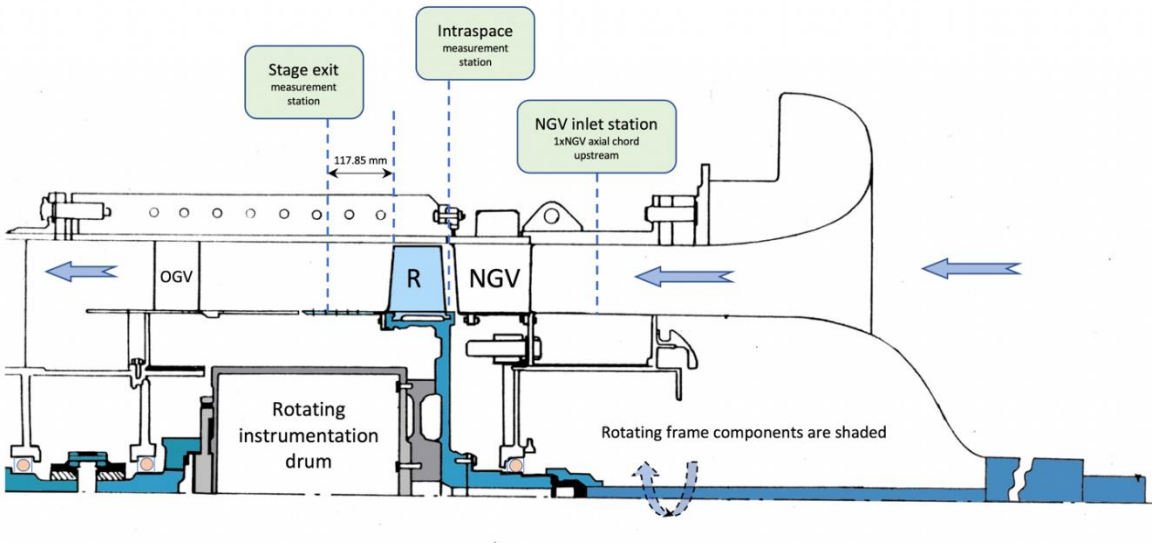

Figure 2-1 AFTRF facility in heat transfer and turbomachinery lab

The apparatus was fabricated in the turbomachinery lab. Vanes and the blades were manufactured using the state of the art blade design techniques. As mentioned earlier,

researchers have not yet completely understood the complexities of the three dimensional flows in a turbine, Sieverding [3]. Using such a test facility can provide a better

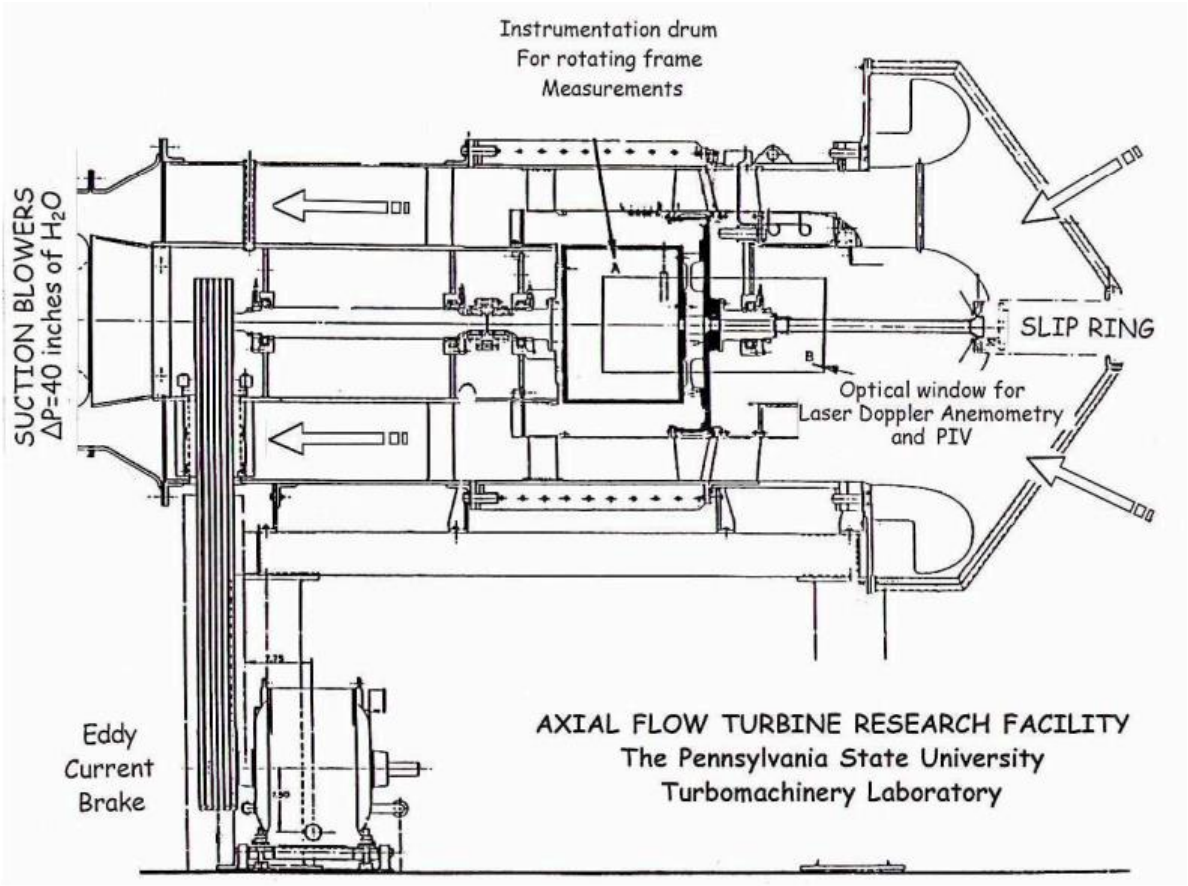

Figure 2-2 AFTRF instrumentation

understanding of these flow characteristics. Various instrumentations have been introduced inside the vanes and blades, some of the typical instruments are shown in Figure 2-2.

The inlet is a large bell-mouth inlet to have maximum air intake with the air filter. As discussed earlier AFTRF has 23 nozzle vanes and 29 rotor blades. The axial spacing between NGV and rotor can be adjusted between 20 to 50% of chord. Flow in the turbine is provided by two auxiliary, adjustable pitch axial fans which are placed in series. These two fans create a pressure rise of 74.7 mm Hg at the volumetric flow of 10.4 m^3/second.

Power generated by the turbine is absorbed by an eddy current brake, as shown in Figure 2-2. Capacity of eddy current brake is up to 60.6 KW. Rotor RPM can also be adjusted within 175 to 1695 RPM and it can be held constant by eddy current break with the tolerance of ± 1 RPM. Rotating probe is used to collect the data in the rotating frame of reference and it is mounted right after the rotor disk. Collected data was transferred to the rotating to stationary transmission system attached to the rotor shaft ahead of the nose cone. A more detailed description of instrumentation is given in Camci [12]

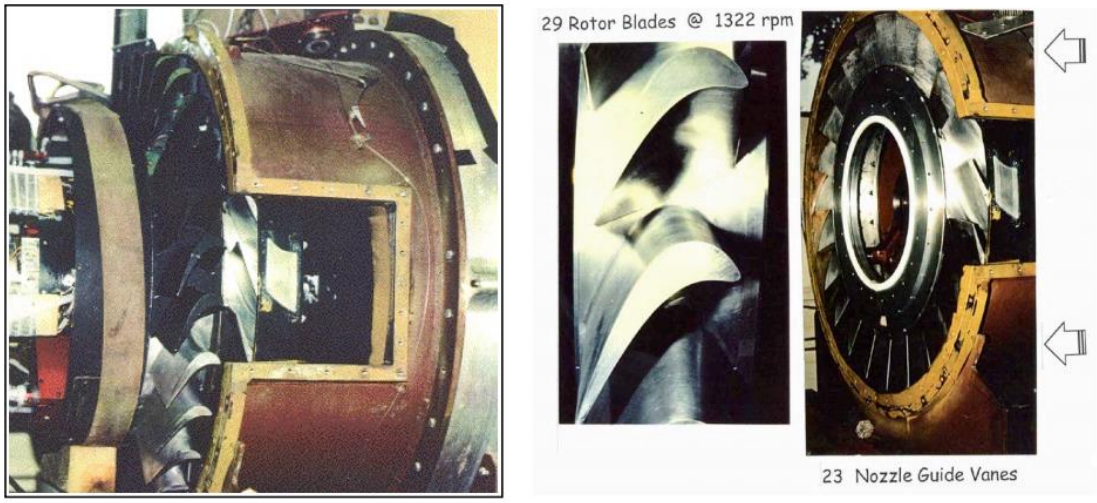

Figure 2-3 AFTRF stage

Figure 2-3 shows the photograph of the facility with removed casing. Midspan section measurement of NGV and rotor are also shown in Figure 2-4

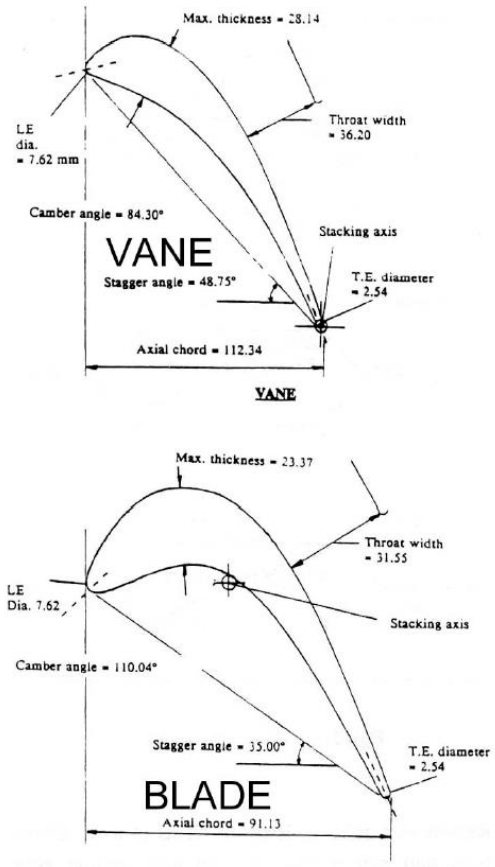

Figure 2-4 Dimension of the vane/blade at the midspan

2.1 Experimental Measurement

The facility contains two traversing mechanisms. One probe traverse unit is mounted right after the rotor disk to give the radial and circumferential measurements in the rotating frame of reference. The second probe is mounted outside the casing of the turbine to measure the absolute flow field data one chord upstream of the nozzle and two chords downstream of the rotor [13]. Static pressure measurements were taken at various locations (h=0.1, 0.2, 0.5, 0.9, etc.) on the NGV and rotor blades by creating static pressure holes at several axial and chord-wise locations. Figure 2-5 shows the various static pressure holes and the instruments on a rotor blade.

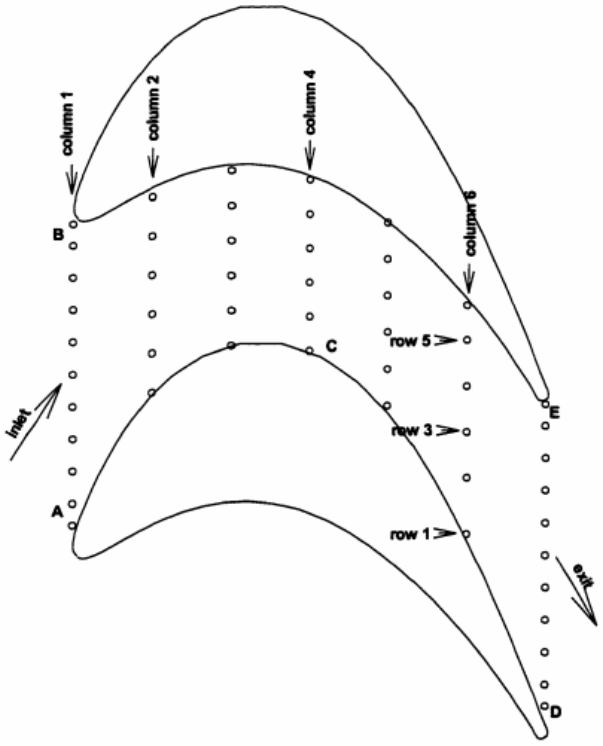

Figure 2-5 Static pressure port on the rotor blade surface

A hot wire probe was used to measure the turbulence intensity upstream of the nozzle. A five-hole probe was used to measure the radial distribution of axial mean velocity at the nozzle inlet. The stagnation pressure was uniform radially. Again, a five-hole probe was used to measure the total and static pressure, radial, tangential, axial, and total velocity magnitudes at a distance of 1.5 chords downstream of the rotor blade. The intra-stage measurements were taken from an axial measurement station located at x/c=1.025 from the leading edge of the NGV. The stage exit measurements were obtained 117.85 mm downstream of the rotor's trailing edge. This distance corresponds to 1.5 times the axial chord (78.57 mm) of the blade tip airfoil.

2.2 Experimental Data and Boundary conditions

The design Performance Parameters are shown in Table 2-1. These experimental conditions were used for the computational validation and more detailed boundary conditions are shown in Table 2-2

Table 2-1 Design performance parameter

Total temperature at the inlet (K)	289
Total pressure at the inlet (kPa)	101.360
Mass flow rate (kg/s)	11.05
Rotational speed (rpm)	1300
Total pressure ratio (P_{01}/P_{03})	1.0778
Total temperature ratio (T_{03}/T_{01})	0.981
Pressure drop(mmHg) (P_{03}-P_{01})	56.04
Power (KW)	60.6
Stator efficiency	0.9942
Rotor efficiency	0.8815
Total-to-Total isentropic efficiency	0.8930

Table 2-2 Detailed boundary conditions used

NGV inlet boundary conditions	
Total pressure (kPa)	101.360
Static pressure (kPa)	100.845
Total temperature (K)	289
Turbulent kinetic energy (TKE)	As shown in Figure 2.6
Velocity magnitude	As shown in Figure 2.6
Rotor exit boundary conditions	
Mass flow rate (kg/s)	11.05
Turbulence intensity (%)	2.2
Turbulence viscous ratio	4
Rotational speed (RPM)	1300

Table 2-3 AFTRF design parameters

Rotor hub tip ratio	0.7269
Tip radius (m)	0.4582
Blade height h (m)	0.1229
Tip relative Mach number	0.24 (max)
Nozzle guide vane	
Number	23
Midspan axial chord (m)	0.1123
Turning angle (deg)	70
Reynolds number based on inlet velocity	$3\sim4 \times 10^5$
rotor-stator axial spacing at hub (mm)	36.32
Rotor Blade	
Number	29
Midspan axial chord (m)	0.0929
Turning at tip angle (deg) Turning angle at hub (deg)	94.42 125.69
Tip clearance t/h	0.8 %
Reynolds number based on inlet velocity	$2.5\sim5.0 \times 10^5$

The above boundary conditions (Table 2-2) closely represent the Zaccaria's experimental data [13]. Inlet velocity and the turbulent kinetic energy are obtained using the Hot Wire probe. Turgut [14] has shown this distribution at one chord upstream of the nozzle guide vanes.

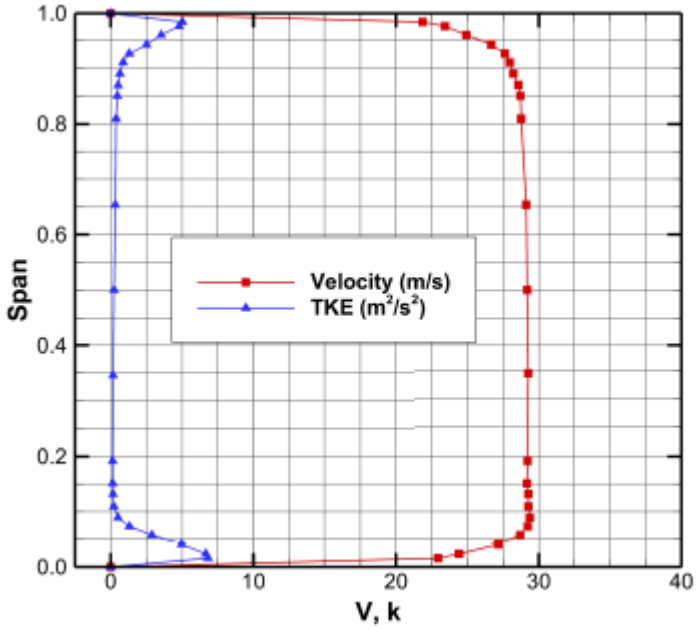

Figure 2-6 Velocity and Turbulent kinetic energy profile at the ngv inlet [14]

2.3 Experimental Data Uncertainty

The assessment of the current computational simulations was performed against a number of measured data sets from the AFTRF. The turbulence intensity at the inlet measurement station, located one chord length upstream of the NGV leading edge, used a single sensor hot wire. The calculated total uncertainty for hot wire measurements was documented as 1.9% in measured turbulence intensity. The turbulent kinetic energy profile was computed to the measured turbulence intensity at the inlet station, assuming an isotropic turbulent flow structure. All three components of the velocity vector in the nozzle guide vane exit flow were measured with a five-hole probe. The relative uncertainty for velocities was calculated as 0.6% for V, 2.5% for Vx, 0.5% for Vθ, and 22% for Vr. A detailed description of the five-hole probe approach is presented in [15]. The uncertainties

for total pressure and static pressure measurements were ±5 Pa. The relative uncertainties on the total pressure and static pressure were 0.03% and 0.033% of the total pressure at the NGV exit, respectively.

The data measurement techniques and associated uncertainties can help in identifying the possible sources of error between the experiment and the computational simulation. The boundary conditions given above were used in the computational model, as presented in Chapter 3.

Chapter 3 **Computational Model**

The development of the computational model is discussed in this chapter. A critical aspect was deciding on the turbulence model to be used during the computational study. The available turbulence models are mentioned in this chapter. Grid/mesh dependence studies were performed on the NGV and the rotor, which were essential to ensure the computational model was correct and validated using the experimental boundary conditions.

3.1 Different Turbulence Model:-

In this simulation, a two-equation turbulence model was used to model the fluid flow. While selecting the turbulence model, the flow transition from laminar to turbulent was considered. The k-omega SST turbulence model [16] was selected along with the Gamma-transition model to effectively predict the flow physics. Details of the boundary conditions were given in Chapter 2. Other turbulence models available in Star CCM+ [17] are given below.

3.1.1 K-Epsilon Model

The K-Epsilon turbulence model is a two-equation model that solves transport equations for the turbulent kinetic energy(k) and the turbulence dissipation rate (ε) in order to determine the turbulent eddy viscosity.

3.1.2 K-Omega Turbulence Model

The K-Omega turbulence model is again a two-equation model that solves transport equation for the turbulent kinetic energy and the specific dissipation rate ‘ω’ in order to determine the turbulent eddy viscosity.

3.1.3 Spalart-Allmaras Turbulence Model

The Spalart-Allmaras turbulence model is one equation model that solves a transport equation for the modified diffusivity in order to determine the turbulent eddy viscosity.

3.2 Mesh and Solid Geometry:-

In this study polyhedral mesh with Prism layers was used. The mesh dependency / grid dependency studies for both NGV and Rotor used the mesh cell size of 1.2 Million, 2.50 Million and 3.2 Million for NGV and 1.6 Million, 3 Million and 5 Million for Rotor. The result of these mesh dependence studies will be discussed later.

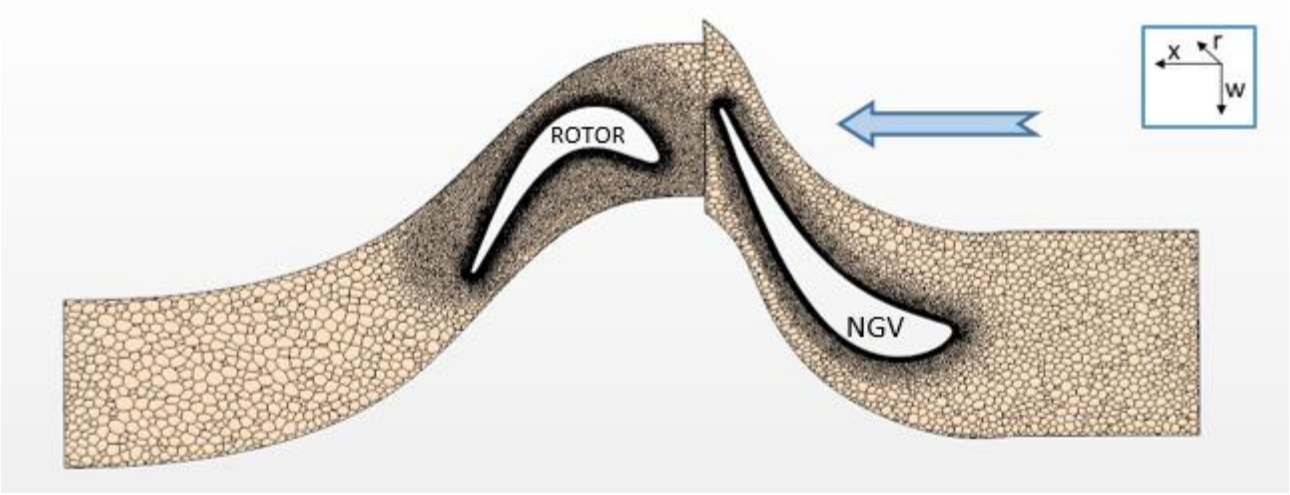

Figure 3-1 Mesh distribution at the midspan of the stage

As shown in Figure 3-1 is the mesh distribution at the midspan of the stage. Around the NGV and rotor blade surface, dark thick lines represent the prism layers. A more detailed image is shown in Figure 3-2. The mesh of the entire stage is shown in Figure 3-3. Using the boundary conditions in Chapter 2 and Mesh cell size of 3.2 Million NGV and 3 Million Rotor resulted in Wall y+ was below 1.

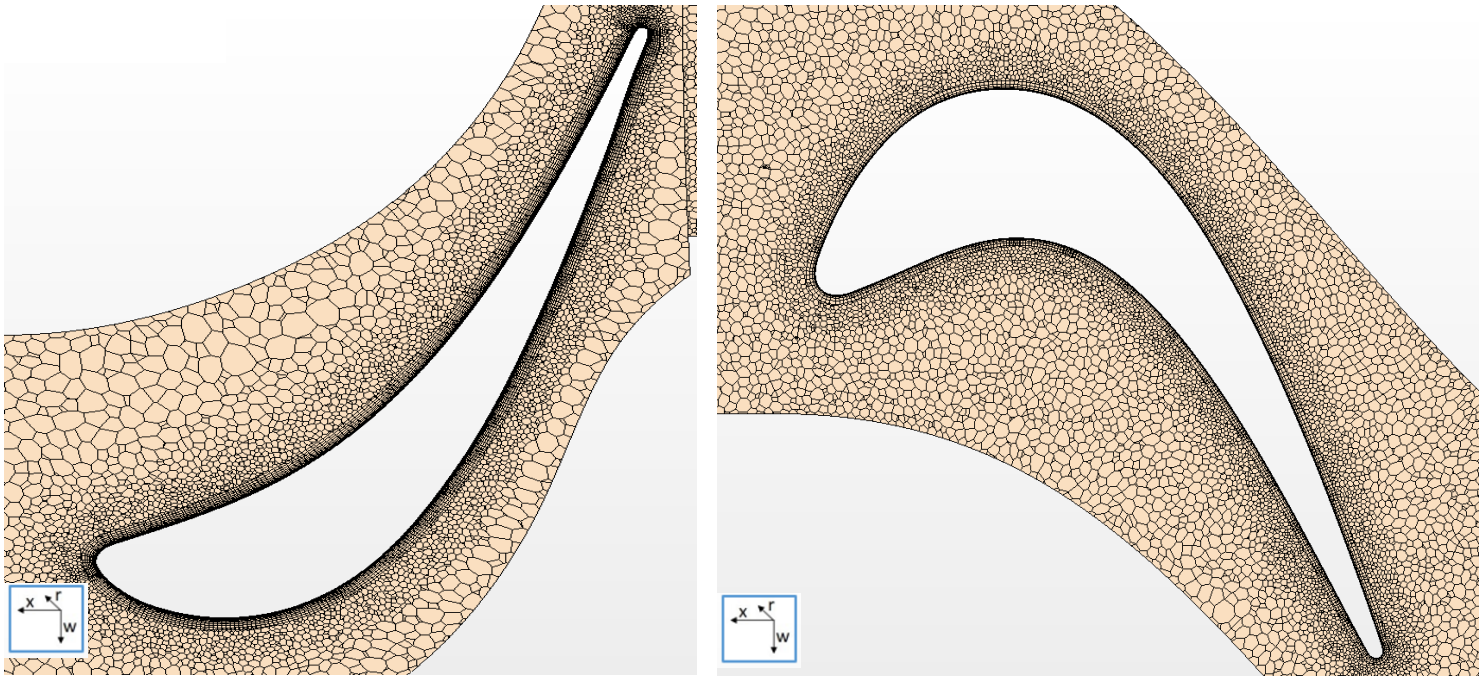

Figure 3-2 NGV prism layers (left) and rotor prism layers (right)

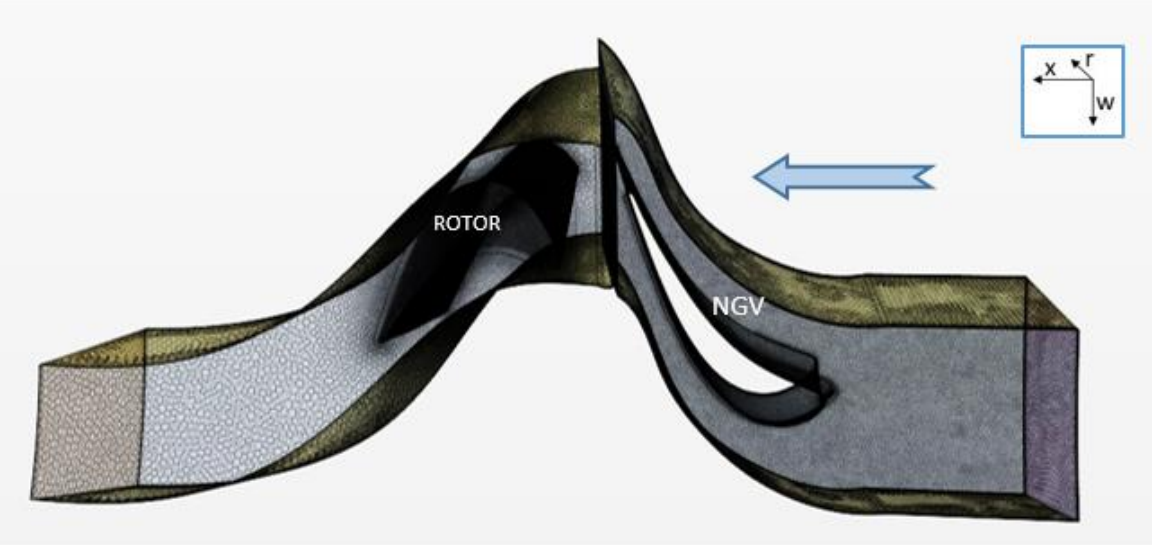

Figure 3-3 Mesh in overall stage

In Star CCM+ there are two major types of meshes: polyhedral and tetrahedral. Tetrahedral cells are easy to generate automatically and are widely used, but cannot be substantially stretched at the boundaries of a surface. Tetrahedral meshes have only four neighbors and computing gradients at the cell centers can be inaccurate and challenging. For example, it is possible that all the neighboring nodes could lie on the same plane or be unevenly distributed around edges of the boundary causing a numerical issue. Polyhedral cells are also easy to generate, but have many neighbors (typically on the order of 10), such that gradient computations can be much better approximated. Even though there are more number of cells, higher computation time can be compensated by the higher accuracy. Polyhedral cells are beneficial for the recirculating flows [18]. Prism layers are introduced

along the walls of NGV and Rotor blades. 15 and 20 prism layers are given around the wall of NGV and Rotor respectively. Unstructured polyhedral cells were used in the current simulation. Using an unstructured mesh provides an advantage when dealing with meshing complex geometries, such as the high turning angles on the NGV and the rotor.

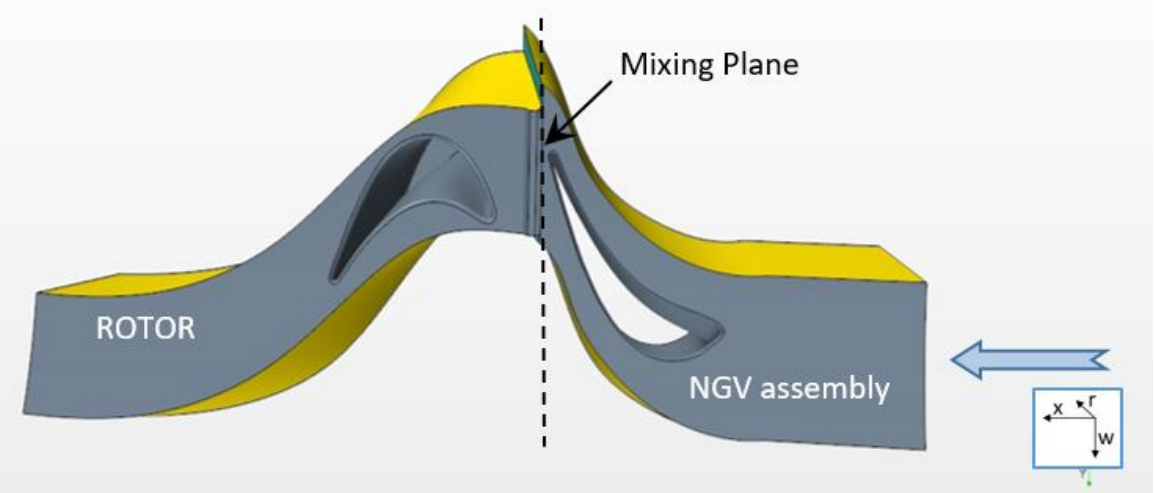

Figure 3-4 Solid geometry of stator-rotor stage

The turbine stage flow simulations were conducted by the general-purpose finite volume flow solver Star CCM+ over a computational domain as shown in Figure 3-4. Three-dimensional RANS flow equations in steady-state were solved for the complete stage (NGV and rotor). The maximum Mach number in this facility was less than 0.3 and which occurred in extremely limited flow zones. Therefore, an incompressible flow solution is obtained. Rotor study is done in the rotating frame of reference whereas NGV is studied in the stationary frame of reference. Interaction space between the NGV exit and rotor inlet is termed as "intra-space" and studied using a "mixing plane" approach which uses "circumferential averaging" to transfer the computational data from NGV to rotor flow

domain. Figure 3-4 and Figure 4-7 show the position of the mixing plane located just downstream of the NGV trailing edge. The mixing plane is parallel to the trailing edge line of the NGV airfoil. The axial position of the measurement station at "intra-stage" is indicated in Figure 2-1. Hub, casing and all flow exposed surfaces of the blade are treated as "adiabatic wall" for the solution of the energy equation.

Inlet boundary conditions are given 1 chord upstream of the NGV and outlet boundary conditions are given 3 chords downstream of the rotor. Inlet is a stagnation inlet and velocity/turbulent kinetic energy for the NGV inlet is shown in Figure 2-6, Stage outlet is mass flow rate type which is given in Table 2-2. Computational model is replica of the Axial Flow Turbine Research Facility, Turbomachinery lab in Hammond Building (College of engineering) with 23 Nozzle guide vans and 29 HP Rotor blades. Using the periodic surface approach it was possible to analyze for the whole stage using only one stator to rotor interaction as shown in Figure 3-4. Rotor blade has tip clearance of 0.8% Figure 3-5

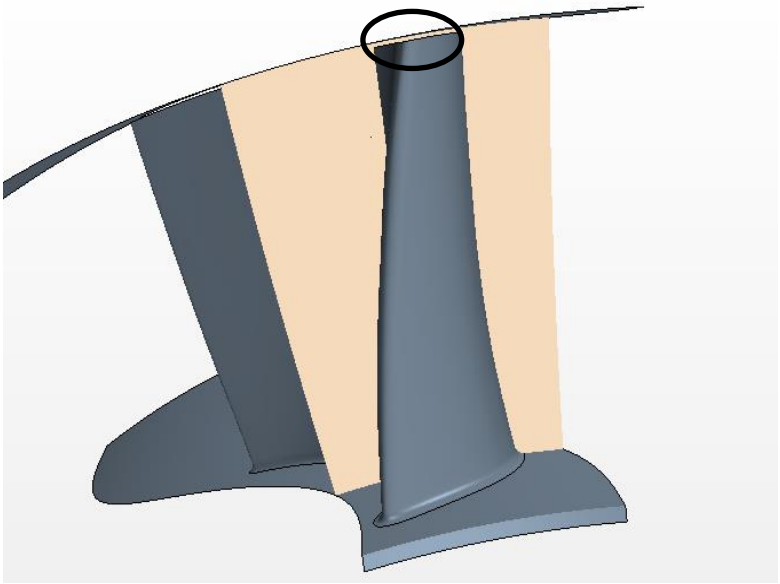

Figure 3-5 Tip clearance (highlighted) between rotor blade and casing

3.3 Gird Dependency study(NGV):-

The grid dependency on NGV blade is done by anlayzing the blade loading at the midspan of NGV (H=0.5). Three different mesh sizes have been selected 1.2Million, 2.5 Million and 3.2 Million. As shown in Figure 3-6, all three meshes were compared against the experimental data. Loading coefficient shows a very similar distribution for all three grid resolution and computational results match well with the experimental results.

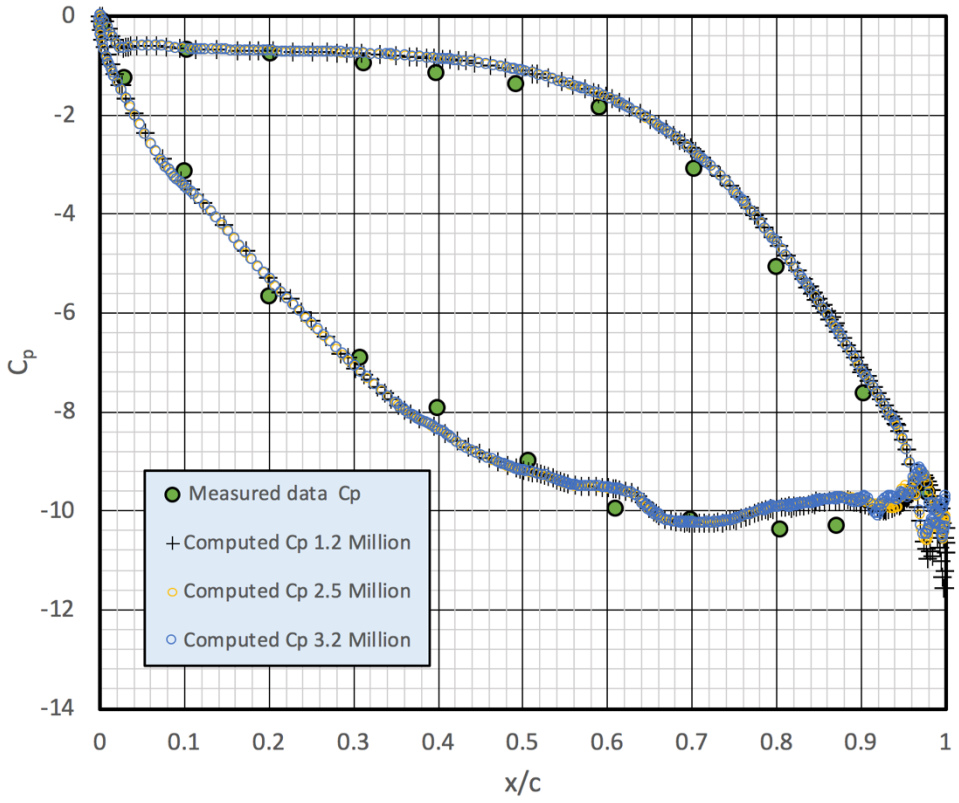

Figure 3-6 Static pressure coefficient at ngv midspan

Static Pressure coefficient is given by the following equation,

$$C_p = \frac{P_1 - P_2}{0.5 * \rho * U_m^2} \tag{3-1}$$

U_m is the blade speed at the mean radius based on the rpm and mean radius value it comes around to be 54.08 m/s. The conclusion of the study was to use the mesh with 3.2 million cells.

3.4 Grid Dependency study (Rotor):-

For the rotor grid dependency study, meshes of 1.6, 3.0, and 5.0 million cells were used. The static pressure coefficient, $C_P{}'$, at the rotor midspan was examined similarly to the NGV study. The grid with 1.6 million cells (as shown in Figure 3-7) showed good agreement with the measured data, except for the mid-chord region on the pressure side between x/c=0.20 and 0.80. The grids with 3.0 and 5.0 million cells both showed very good agreement with the experimental data on both the pressure side and the suction side of the rotor airfoil. The experimental loading data, C_p', for the rotor was obtained from pressure transducers in the rotating instrumentation drum of the AFTRF, as shown in Figure 2-2

Static pressure coefficient at the rotor midspan is given by the following formula,

$$C_p{}' = \frac{P_2 - P_{3avg}}{0.5 * \rho_2 * W_{x2,avg}^2} \qquad (3\text{-}2)$$

For rotor it was decided that 3 Million cells grid size is optimum.

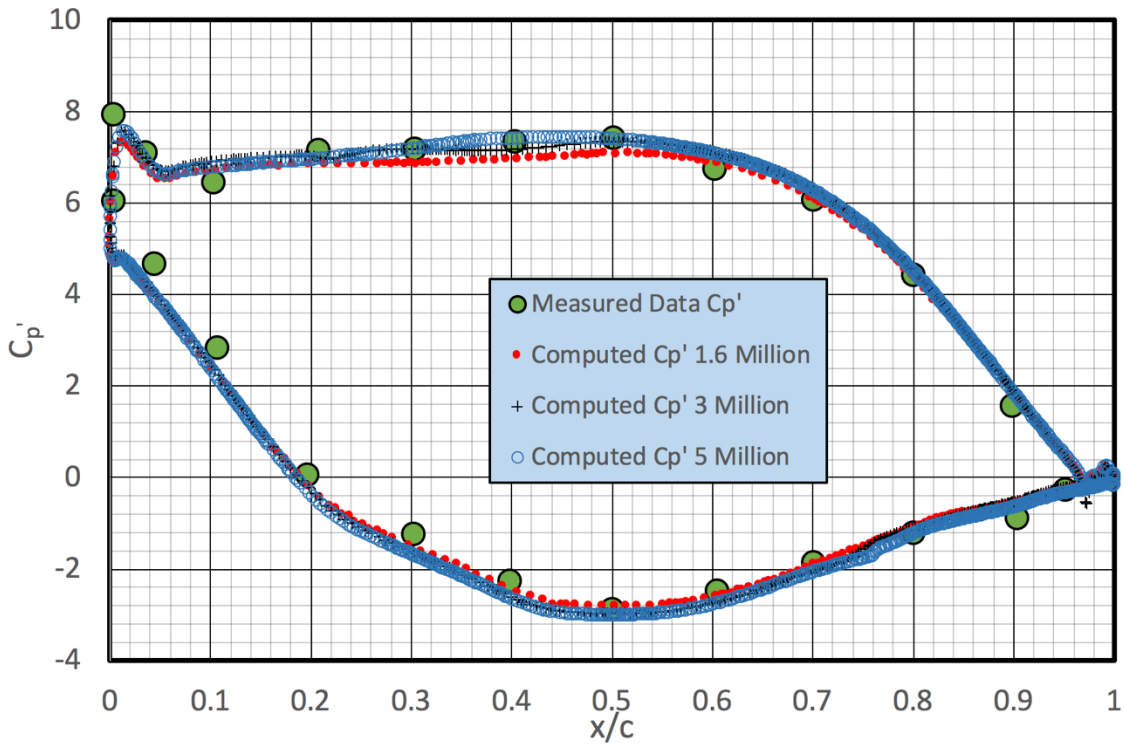

Figure 3-7 Static pressure coefficient at rotor midspan

To get proper validation it is essential to make sure the computer model is correct, from this chapter mesh type and cell size, and turbulence model were selected. Using the grid dependency study, number of cells for NGV and the rotor were decided.

Chapter 4 **Nozzle Guide Vane (NGV) and Rotor Validation**

Various parameters like Total pressure coefficient, Static pressure coefficient and exit velocity profiles for both NGV and Rotor are compared in this chapter. Experimental data collected from the sensors/probes mentioned in Chapter 2 were used to validate the computational result. All the computational measurements for NGV were taken at the same location as in the experiment (x/c=1.025). For the rotor inlet, the plane was located at x/c=1.018 and the rotor exit plane was located at x/c=1.5 downstream of the rotor. Based on the computer model and the final grid size in Chapter 3, further validation was performed.

4.1 NGV Validation

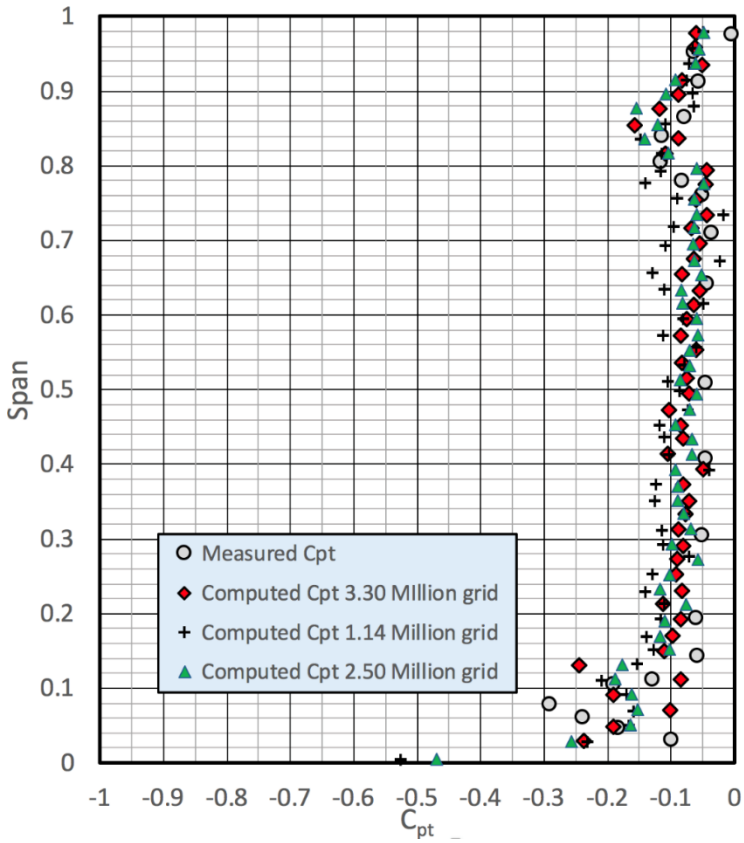

Figure 4-1 Total pressure coefficient at ngv exit

Figure 4-1 shows the total pressure coefficient (equation 4-1) distribution at the NGV plane, which is located at x/c=1.025. The total pressure coefficient plot has also been used to show the grid dependency. Meshes containing 1.14, 2.50, and 3.30 million cells were all considered. The 3.30 million cell grid predicted the nature of the plot well within acceptable limits.

Total pressure is given by the equation,

$$C_{pt} = \frac{P_{02} - P_{01}}{0.5 * \rho * V_1^2} \qquad (4\text{-}1)$$

The total pressure coefficient was normalized using the axial mean velocity at the inlet of the NGV. The rim seal effect or the leakage in the wheel space cavity can cause deviations in the plot near the hub at h=0.0 (Span=0.0). From 20% to 80% span, C_{pt} computations were in accordance with the experimental data. The total pressure coefficient near the casing deviated slightly, which could be because there was an open slot for the probe to transverse. This opening creates suction near the casing, reducing the losses, thus the computation showed greater losses. Figure 4-2 shows the location of the measuring plane.

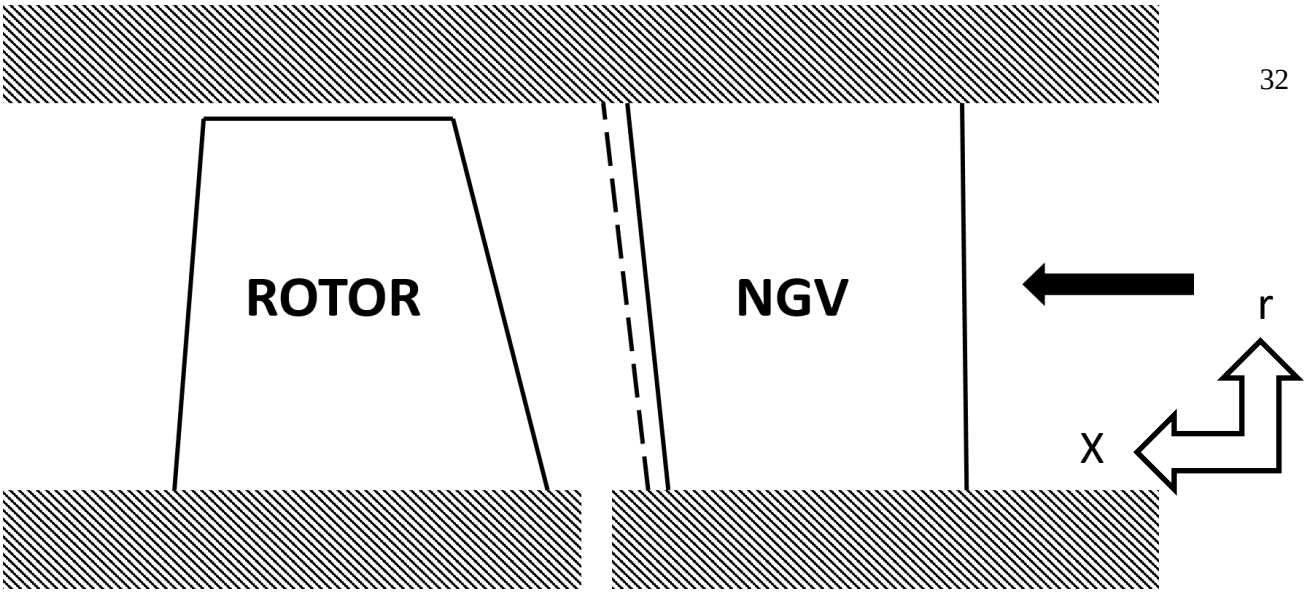

Figure 4-2 NGV exit plane location at x/c=1.025

Figure 4-3 shows the rim seal flow/wheel space cavity. There is a mass flow leakage through the rim seal cavity. In current computation the cavity has been treated as wall but previous computations by Turgut [14]. Exact mass flow rate coming out from the seal cavity is not measured so there is no fixed value for that. By varying the mass flow rate from 0.50% of the inlet mass flow to 1.25% of the inlet mass flow, Turgut shows that secondary flow rises in the radially outward direction hence shifting the C_{pt} peak, it increases in the radial direction by increase in the mass flow rate.

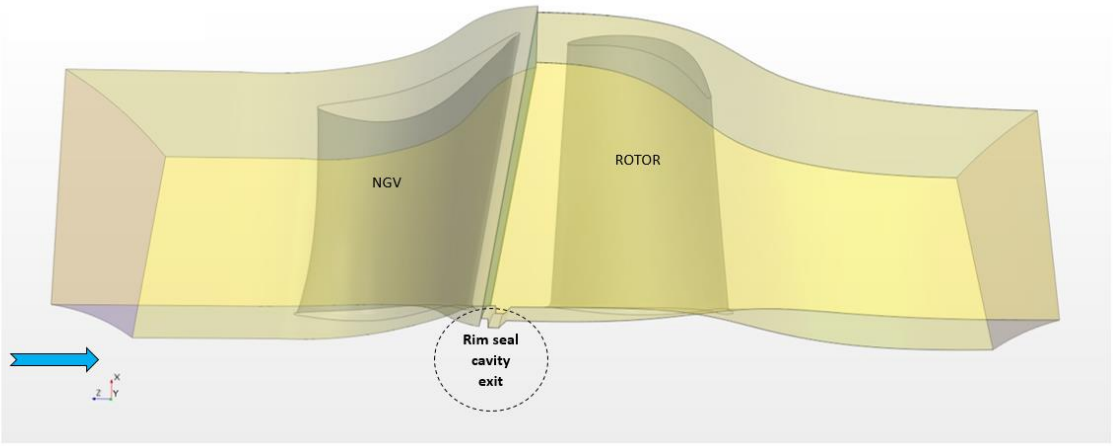

Figure 4-3 Provision for wheelspace/rim seal cavity exit at the intraspace between ngv and rotor

Figure 4-4 compares the computational and experimental velocities, using the axial, radial, and tangential components. Computational axial velocity was a good match with experimental data, such that the mass flow rate remained almost constant. The radial component remained close to zero. However, there was deviation between the experimental and computational tangential velocity components. There was a decrease in the tangential velocity; the maximum decrease (6%) was noted at the 30% span location. This decrease in velocity was supported by an incerase in the static pressure, as shown in Figure 4-5. Note that the experimental data does not begin at 0.00, nor does it end at 1.00, because of the probe. It was not possible in the current experimental facility to measure the parameters directly on the hub or on the casing.

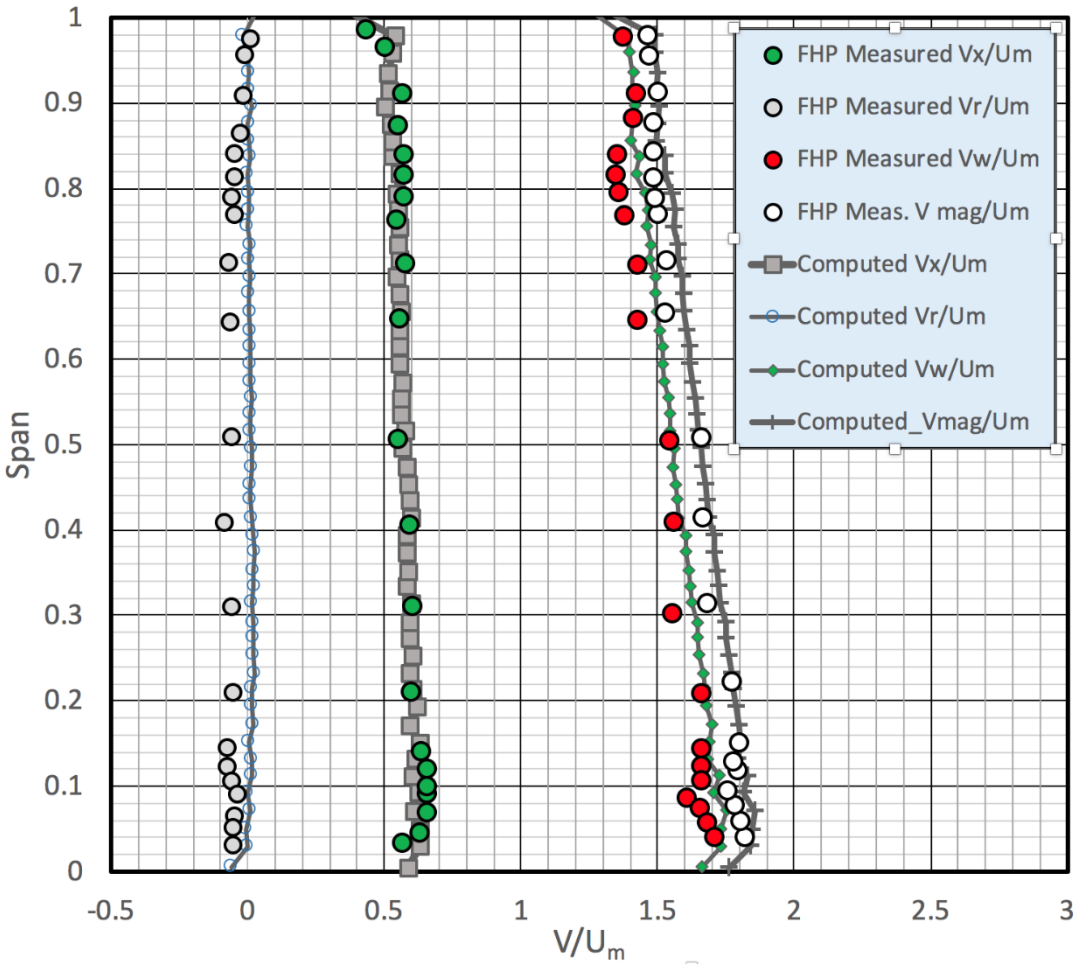

Figure 4-4 Velocity components at ngv exit

Figure 4-5 compares the computational and experimental static pressure coefficient, which is given by the following equation:

$$C_p = \frac{P_1 - P_2}{0.5 * \rho * U_m^2} \qquad (4\text{-}2)$$

Computational data was in good agreement with the experimental data. Above 30% span and below 80% span there was an increase in static pressure coefficient, due to a decrease in velocity. Changing the RPM from 1300 to 1330 shifted the curve closer to the

experimental values. From equation 4-2, it can be seen that the blade speed at the mean radius has a higher influence on the static pressure coefficient than the static pressure differential.

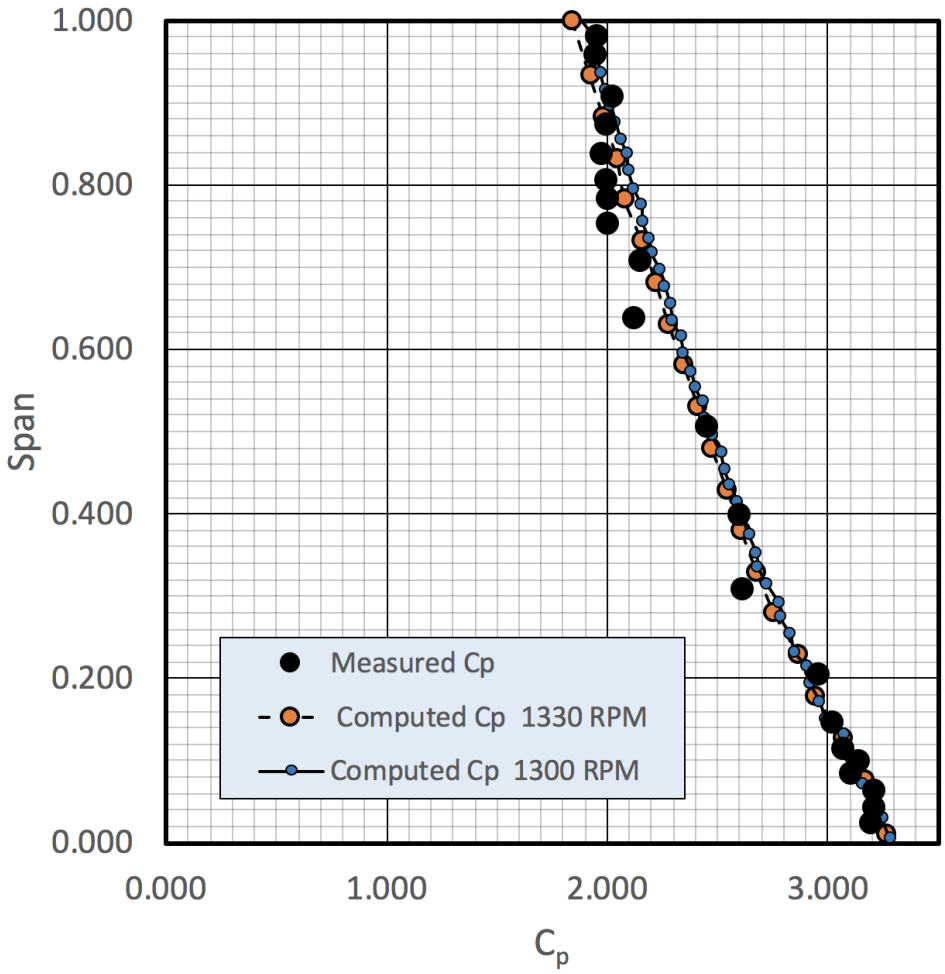

Figure 4-5 Static Pressure coefficient at the ngv exit

4.2 Rotor Validation

Figure 4-6 , shows the total pressure coefficient at the rotor inlet. The rotor inlet plane is perpendicular and located at x/c=1.018 from the casing trailing edge. Figure 4-7 shows the location of the rotor inlet measuring plane and the mixing plane. Total pressure coefficient is given by the following equation:

$$C_{pt} = \frac{P_{02} - P_{01}}{0.5 * \rho * V_1^2} \qquad (4\text{-}3)$$

Computational data was in good agreement with experimental data for most of the span, but it deviated below 20% span. This deviation can be attributed to the wheelspace or rim seal cavity, as shown in Figure 4-3. Turgut [14] has also shown that the computational curve moved closer to the experimental curve with an increase in the seal flow.

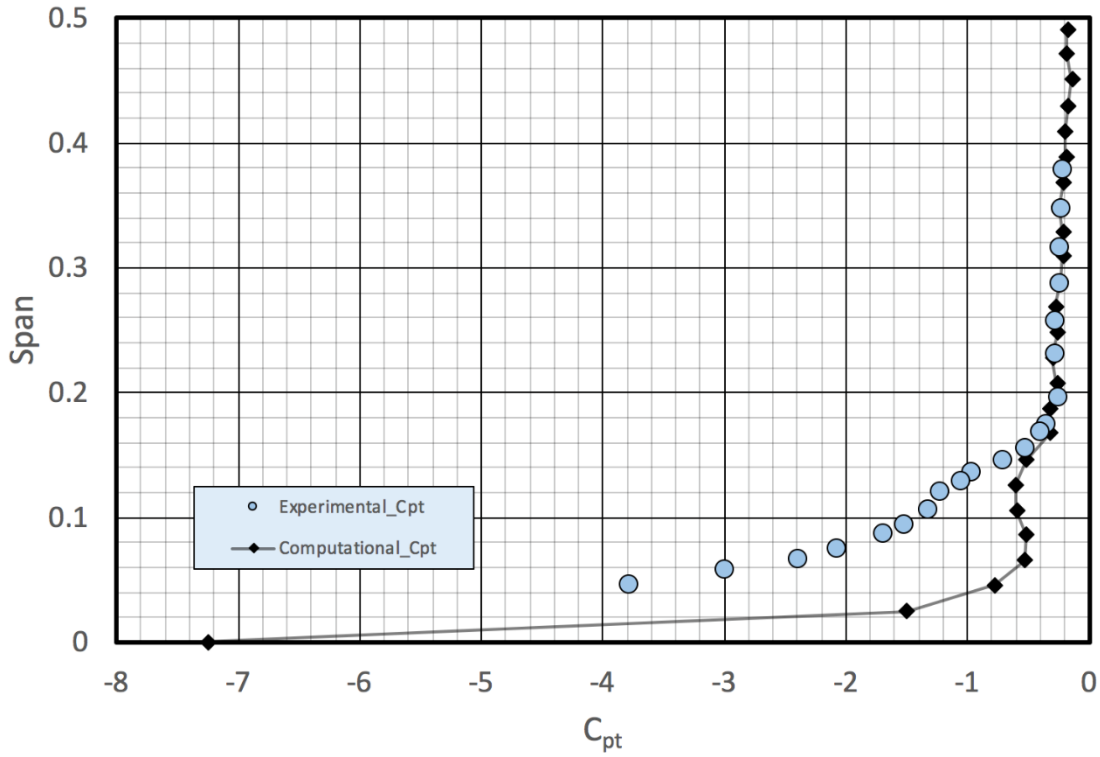

Figure 4-6 Total pressure coefficient at rotor inlet plane

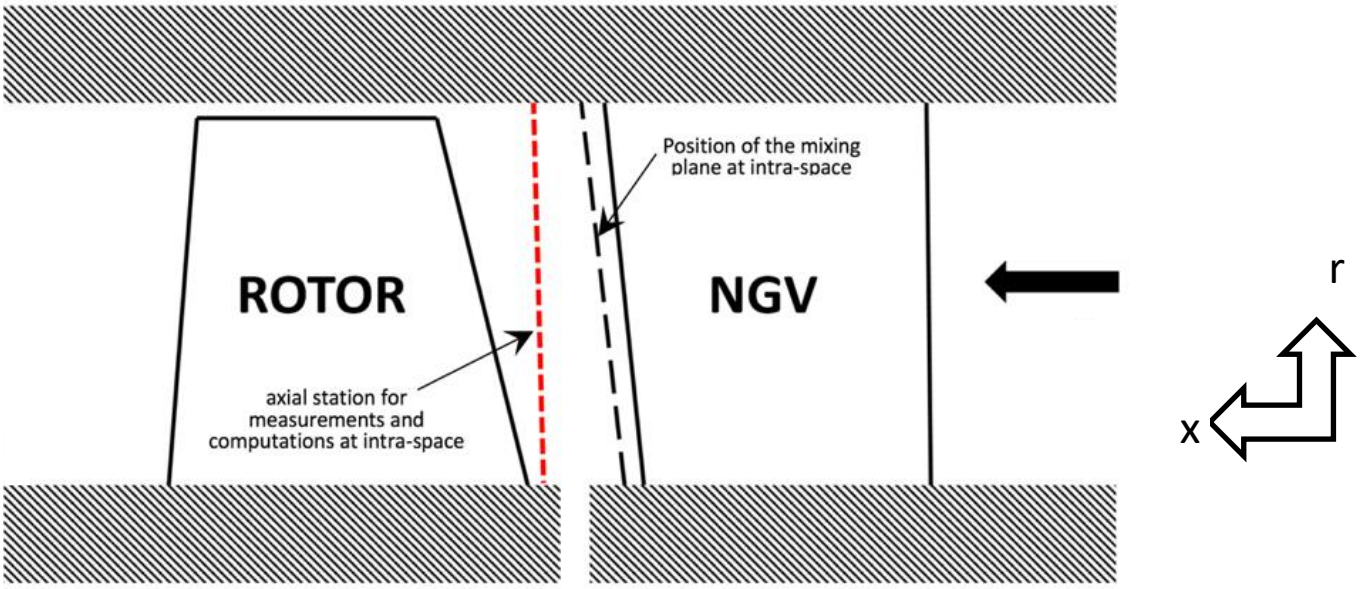

Figure 4-7 Location of rotor inlet plane and intraspace mixing plane location

The rotor exit profile is shown in Figure 4-8, it is measured at x/c=1.5 downstream of the rotor trailing edge. Data was collected from five-hole probe. Computational radial velocity component matches really well with experimental results. Tangential and axial components did not agree well with the experimental results from 20% to 60% of the span. The axial component of the velocity was directly related to the mass flow rate. According to Figure 4-8, the computation under-predicted the mass flow rate. This could be because of the turbulence model that was selected for the computation or it could be other CFD limitations, such as flow dissipation occurring quicker than in the experimental environment.

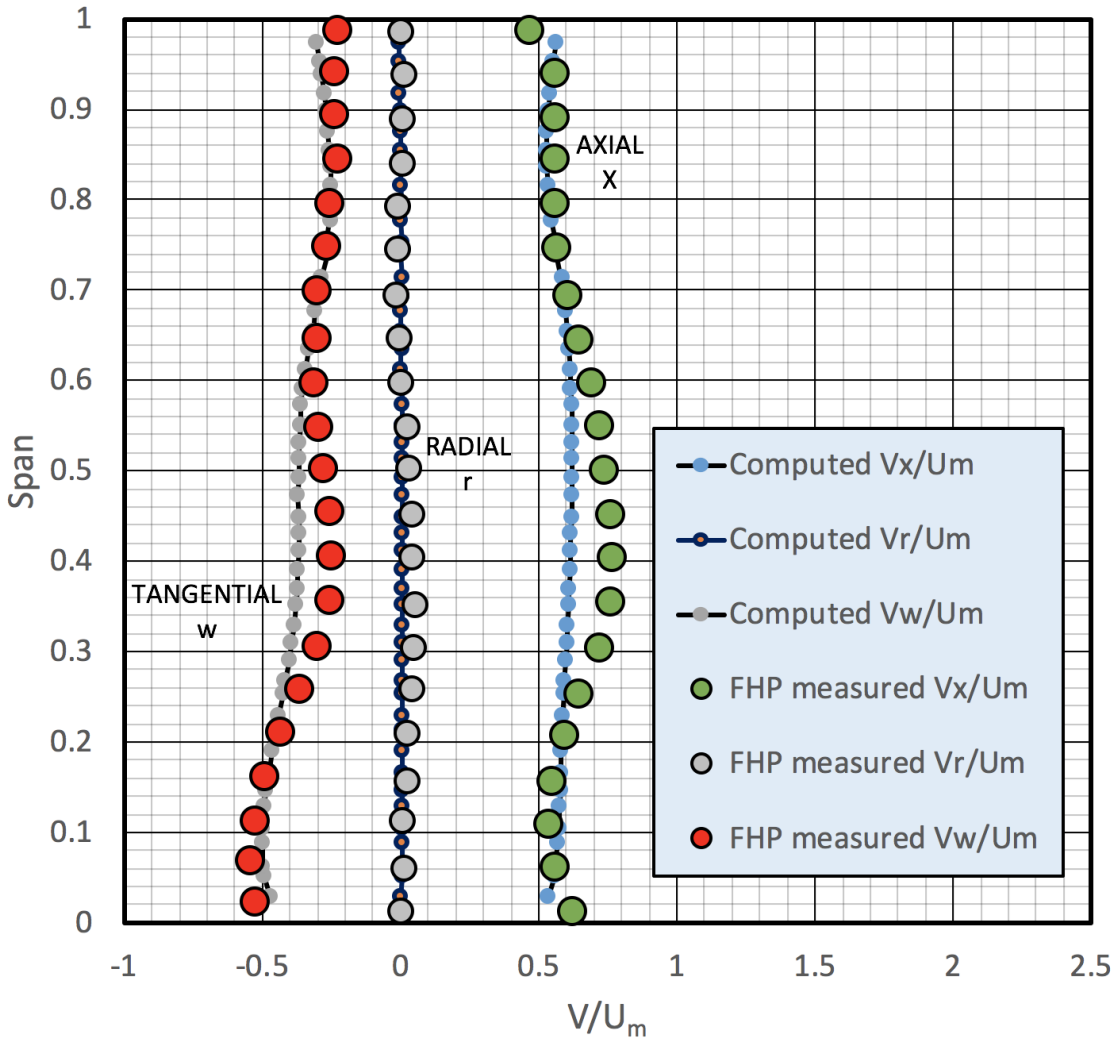

Figure 4-8 Velocity components at rotor exit

The span region from 20% to 60% was also dominated by secondary flows, including the horseshoe vortex, the passage vortex, and the leading edge vortex. It is possible that the turbulence model or the mesh quality could not properly capture the secondary flows and wake regions.

Blade loading-

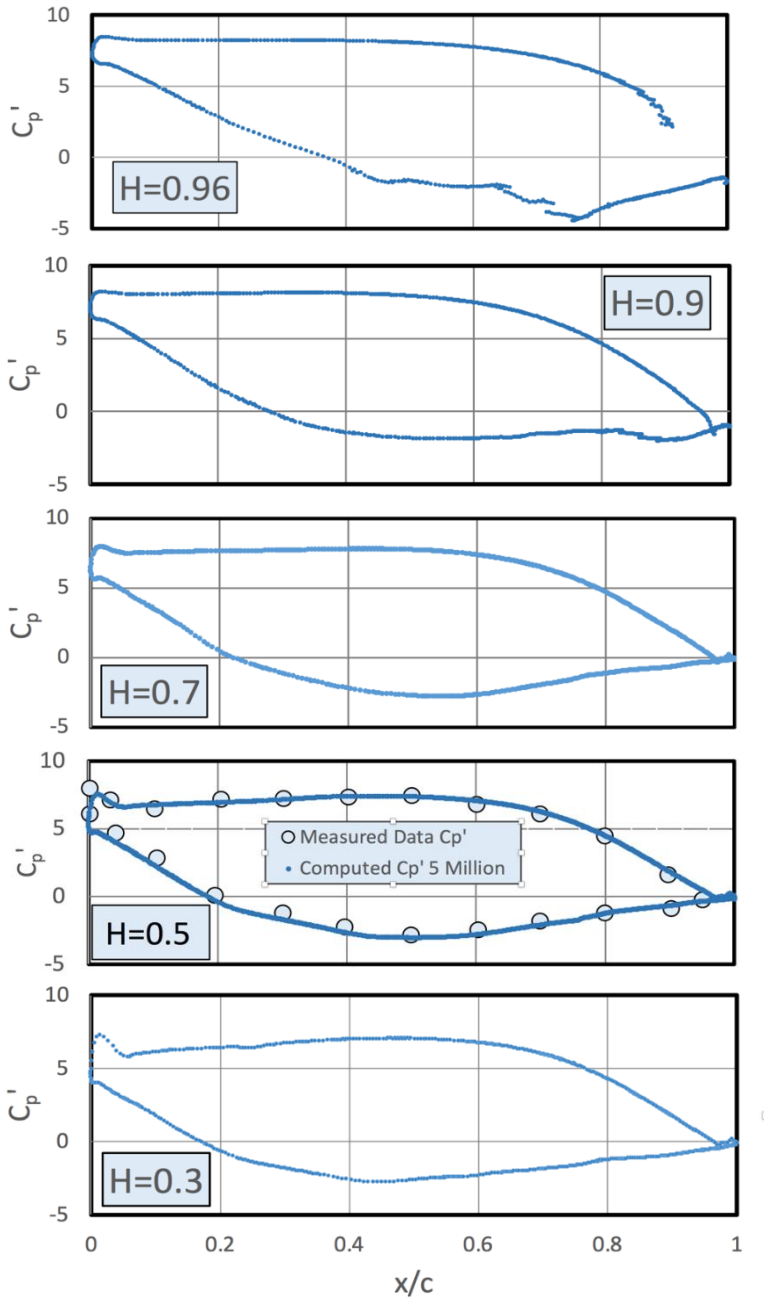

Figure 4-9 Blade loading for rotor at different H location

Blade loading provides a basic understanding of the pressure distribution on the suction and pressure sides of the blade. The midspan static pressure coefficient was compared to the experimental data. As discussed in Chapter 1, secondary flow decreased the lift/net-work output by decreasing the gap between the pressure side and the suction side. For a span of H=0.3, there were more secondary flow losses than at H=0.5. Further away from the hub and closer to the casing (H=0.9, 0.96), it can be seen that the flow was more dominated by the tip leakage vortex. As discussed in Section 1.3, the tip leakage vortex was formed because of the pressure difference between the pressure side and the suction side. This leakage vortex results in the maximum pressure loss, as compared to any other secondary flows.

Figure 4-10 shows the static pressure drop at span locations closer to the tip region, specifically at H=0.9, 0.93, 0.96, and 0.97.

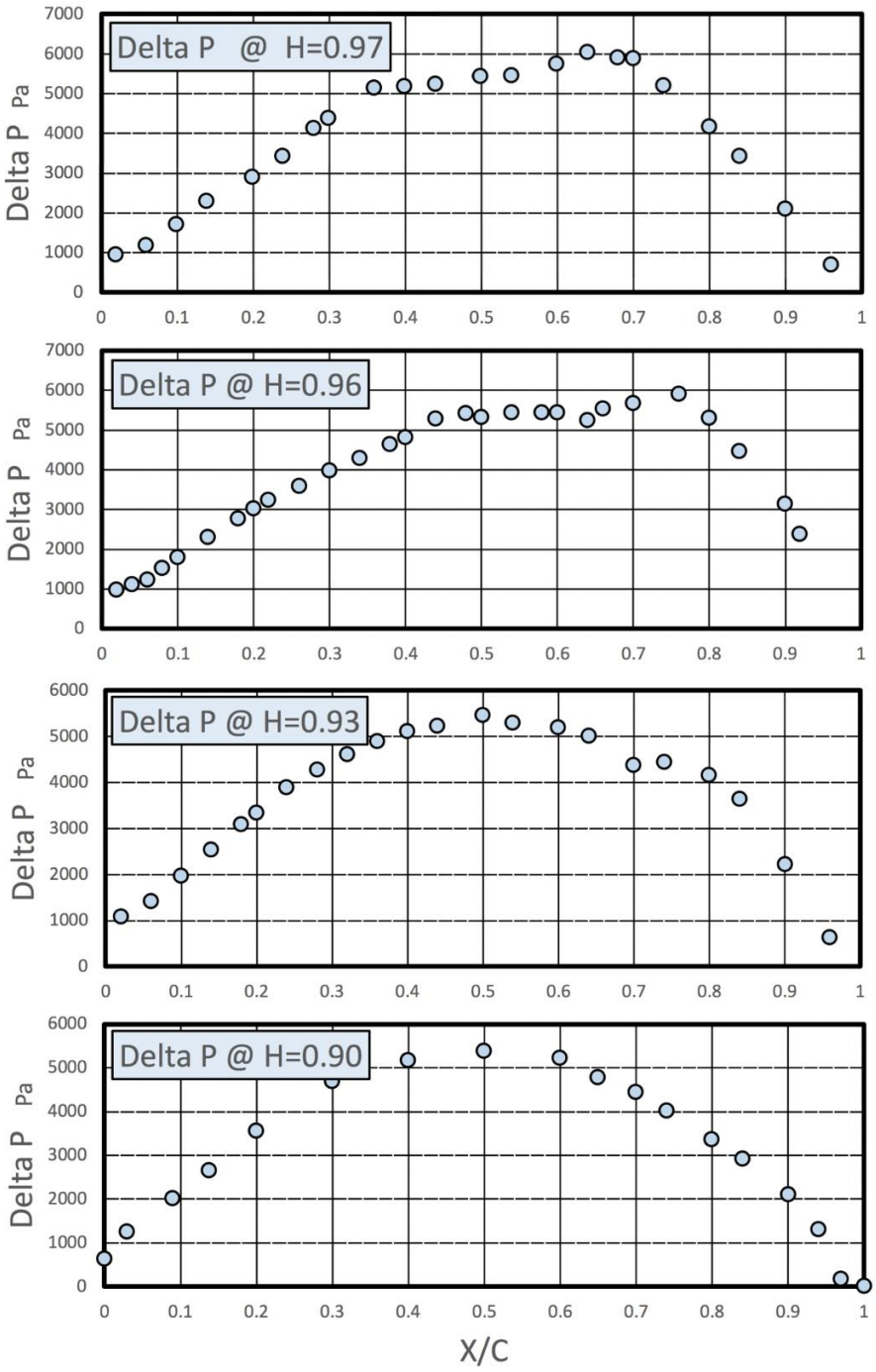

Figure 4-10 Static pressure drop at different span location

Purpose of this research was to computationally validate the NGV and the rotor, this chapter dealt with the validation in detail. Validation results look promising so now total-to-total efficiency can be compared in the coming chapter.

Chapter 5 **Stage Efficiency**

Total-to-total efficiency (η_{tt})/isentropic efficiency/stage efficiency is a direct measure of the losses that occur in a turbine passage. The losses contain the secondary flows and tip leakage vortex discussed in Section 1.3. To compute this efficiency, the turbine stage/stage total pressure ratio and the total temperature ratio were used. A simple case study is included in this chapter to determine the effect of changing the stage total temperature ratio. The case study compares a low pressure turbine (AFTRF) and a high pressure turbine. Plots are now discussed based on the stage inlet and stage exit. The inlet is located one chord upstream of the NGV and the exit is located 117.85 mm downstream of the rotor trailing edge, near the casing.

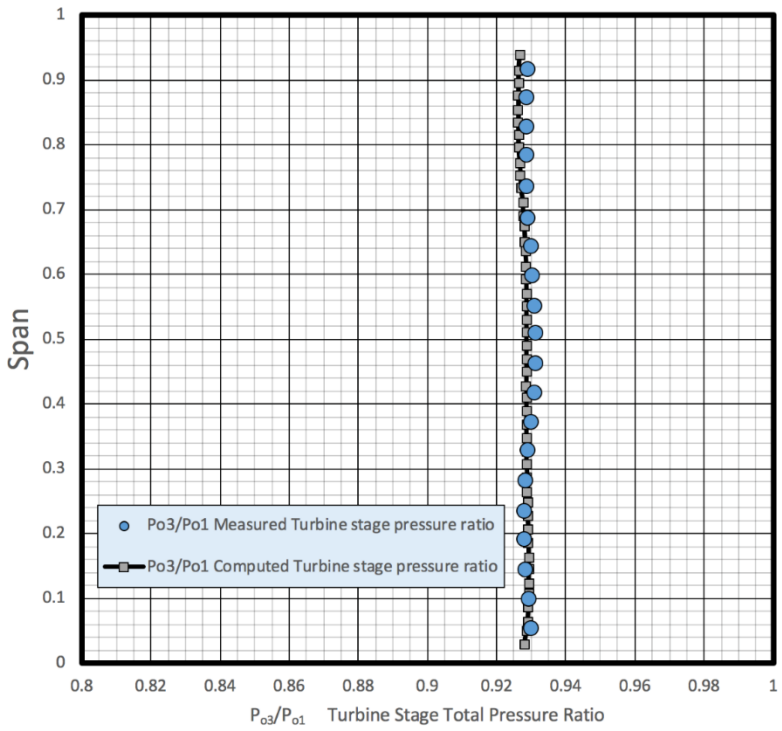

Figure 5-1 Turbine stage total pressure ratio

P_{01} Was taken as 101360 Pa (Table 2-2). The computational and experimental data were in good agreement, as shown in Figure 5-1. It is critical to note that due to the probe limitations, data at a span of 0% and 100% have not been recorded.

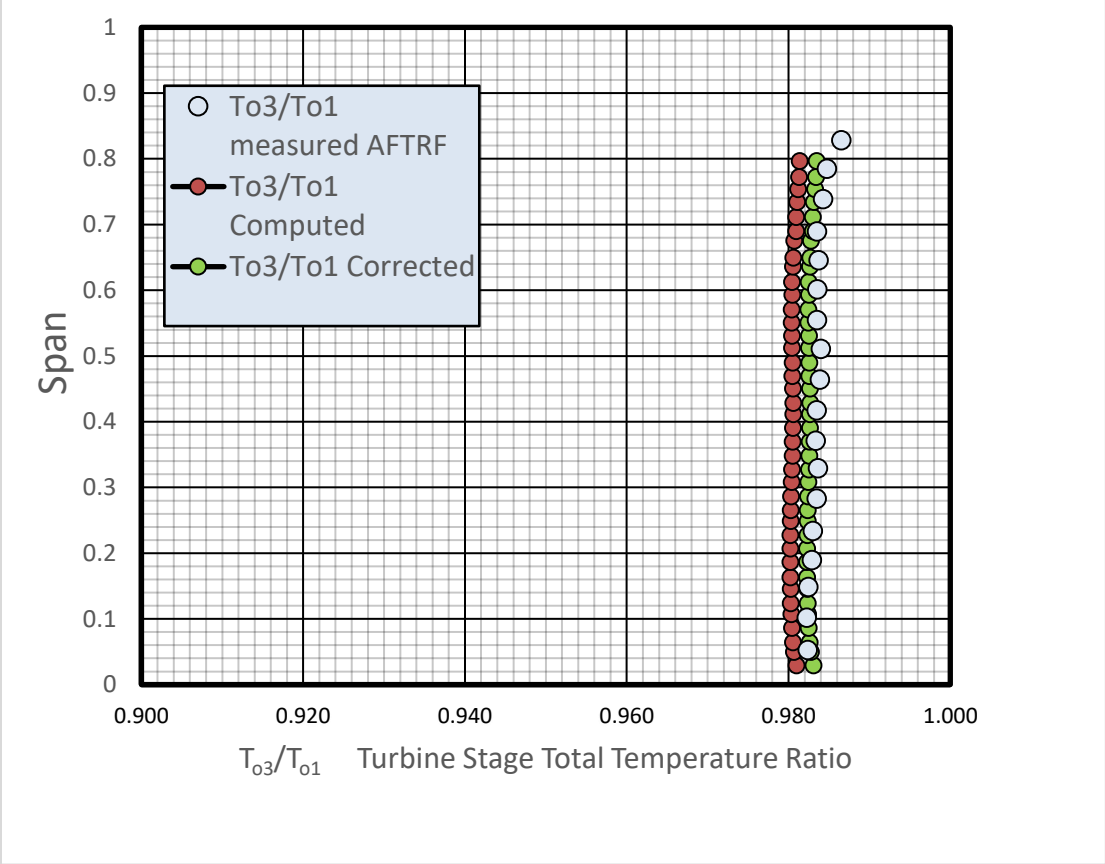

Figure 5-2 Turbine stage total temperature ratio

Figure 5-2 shows the total temperature ratio of the turbine stage. The computational temperature ratio was lower than the experimental ratio. Because of this, the computational efficiency was higher than the experimental efficiency. T_{01} was given as 289 K (Table 2-2). By increasing the exit total temperature by 0.6 K, the total temperature curve shifted toward the experimental curve. The reason why the computational model was under predicting the temperature at the rotor exit could be due to the viscous effects in the rotor, which would

result in an increased temperature drop. The total temperature ratio was reduced near the hub and the casing, as compared to 20% to 60% of the span. Increased total temperature, turbulent kinetic energy and viscous dissipation in the boundary layer would also cause the lower efficiency numbers.

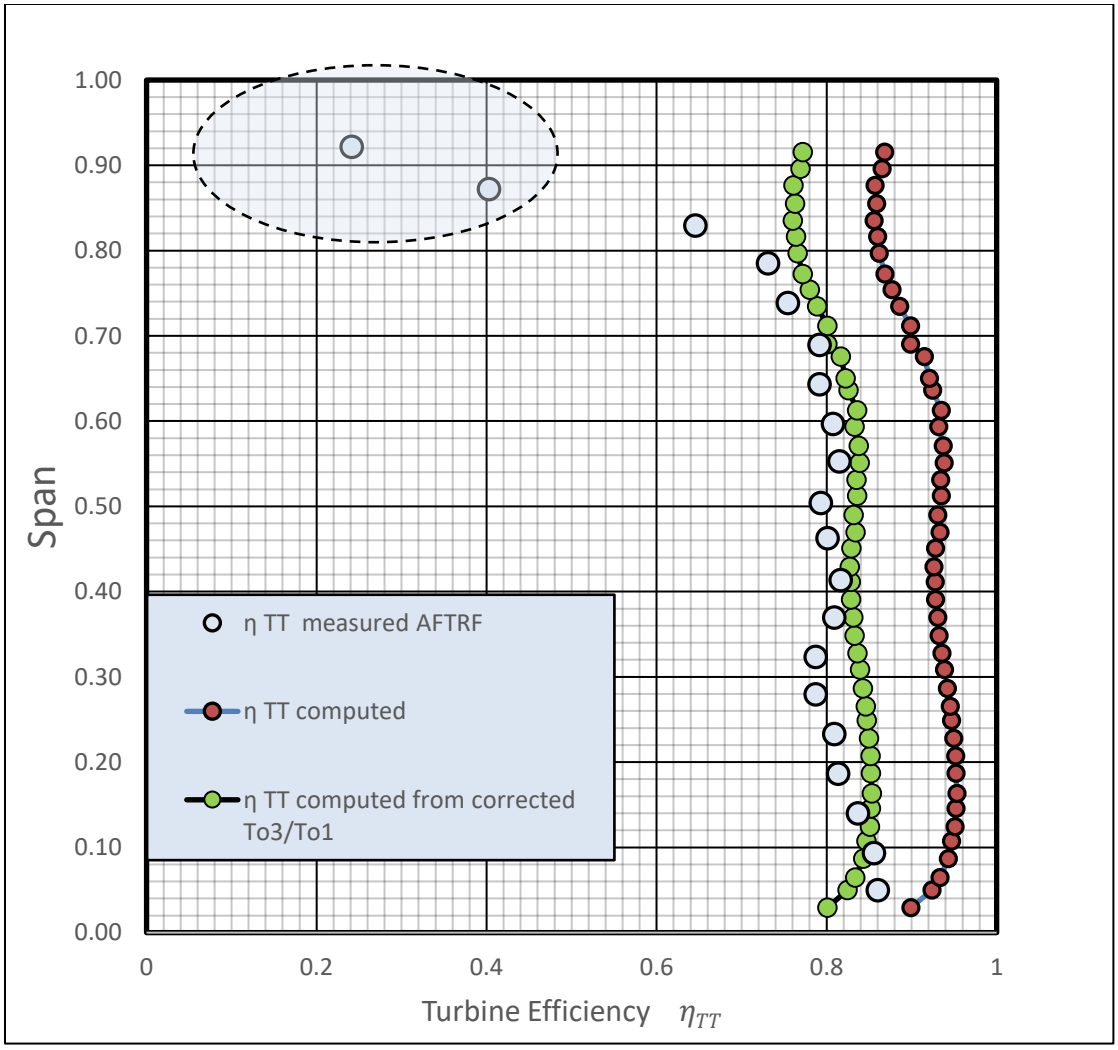

Figure 5-3 Total-to-total efficiency

Figure 5-3 shows the total-to-total efficiency both computational and experimental of the AFTRF stage. The calculation of total-to-total efficiency is given by the following equation,

$$\eta_{tt} = \frac{1-\frac{T_{03}}{T_{01}}}{1-\left(\frac{P_{03}}{P_{01}}\right)^{\frac{\gamma-1}{\gamma}}} \qquad (5\text{-}1)$$

As seen in equation 5-1 total-to-total efficiency is dependent on the overall turbine total temperature ratio and turbine total pressure ratio. Figure 5-2 showed that minor changes in the temperature (0.6 K) can have a lasting impact on the temperature ratio. The effect of the temperature ratio on the total-to-total efficiency can be seen in Figure 5-3. On average, there is a shift of 0.0982 or 9.82% when increasing the stage exit temperature by 0.6 K.

The following section provides better understanding of how a minor change in temperature can affect the efficiency plot. Two different cases are presented: one is of the AFTRF (low pressure (LP) turbine) ($\frac{P_{03}}{P_{01}} = 1.07$) and a generic high pressure (HP) ratio ($\frac{P_{03}}{P_{01}} = 0.5$). δT_{03} (Temperature measurement error) varied from 0 to 2 K and δP_{03} (Pressure measurement error) varied from 0 to 100 Pa

Figure 5-4 shows the change in the temperature measurement error on the x- axis.

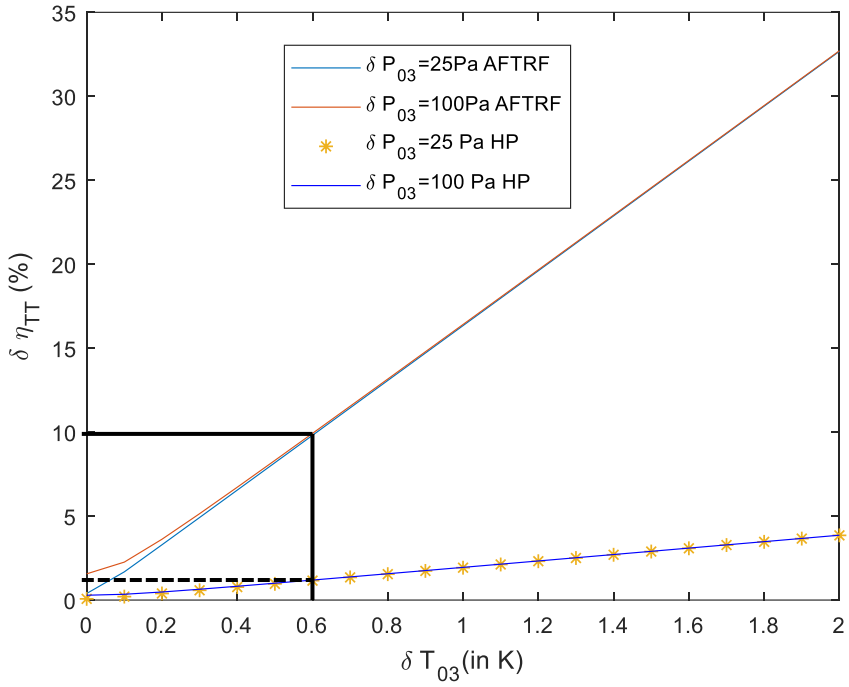

Figure 5-4 Efficiency dependency against the temperature change

Considering the current case (temperature measurement error of 0.6 K), the change in efficiency is nearly 0.1 (10%), which is close to the expected value from Figure 5-3 (0.0982 or 9.82%). The same effect was seen for the HP turbine, but for a smaller value of 0.01 (1%). Figure 5-5 shows that a change in δP_{03} did not have any significant effect on the efficiency plot for both HP and LP turbines. Two different δP_{03} values of 25 Pa and 100 Pa were investigated for both LP and HP turbines. Figure 5-4 shows that even if the δP_{03} value varied from 25 Pa to 100 Pa, the same line was followed for both LP and HP cases.

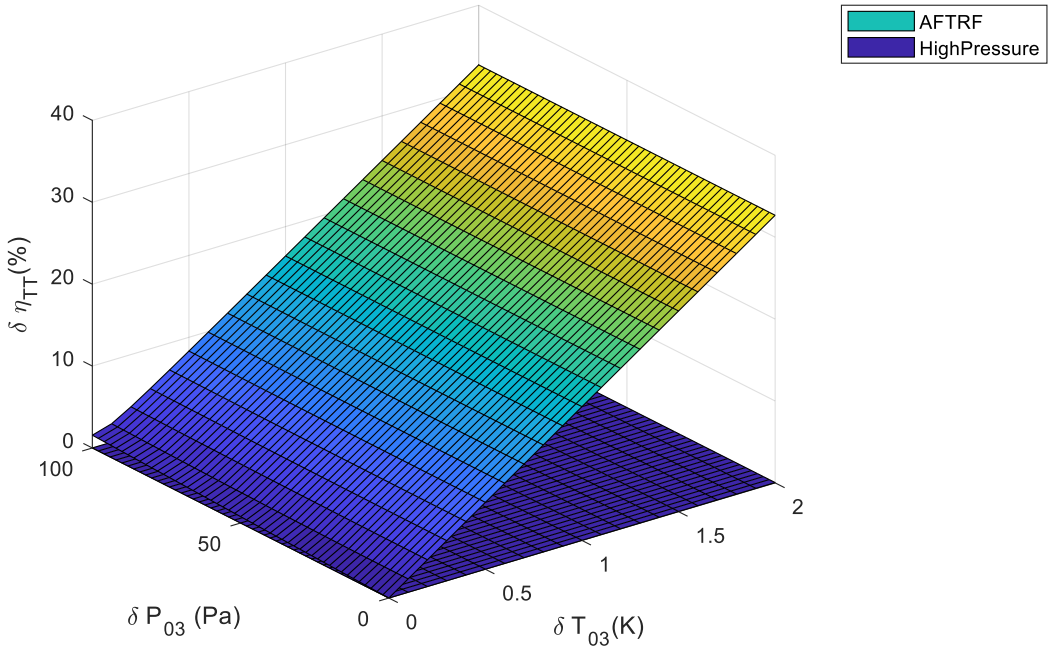

Figure 5-5 3-D plot for efficiency, temperature and pressure

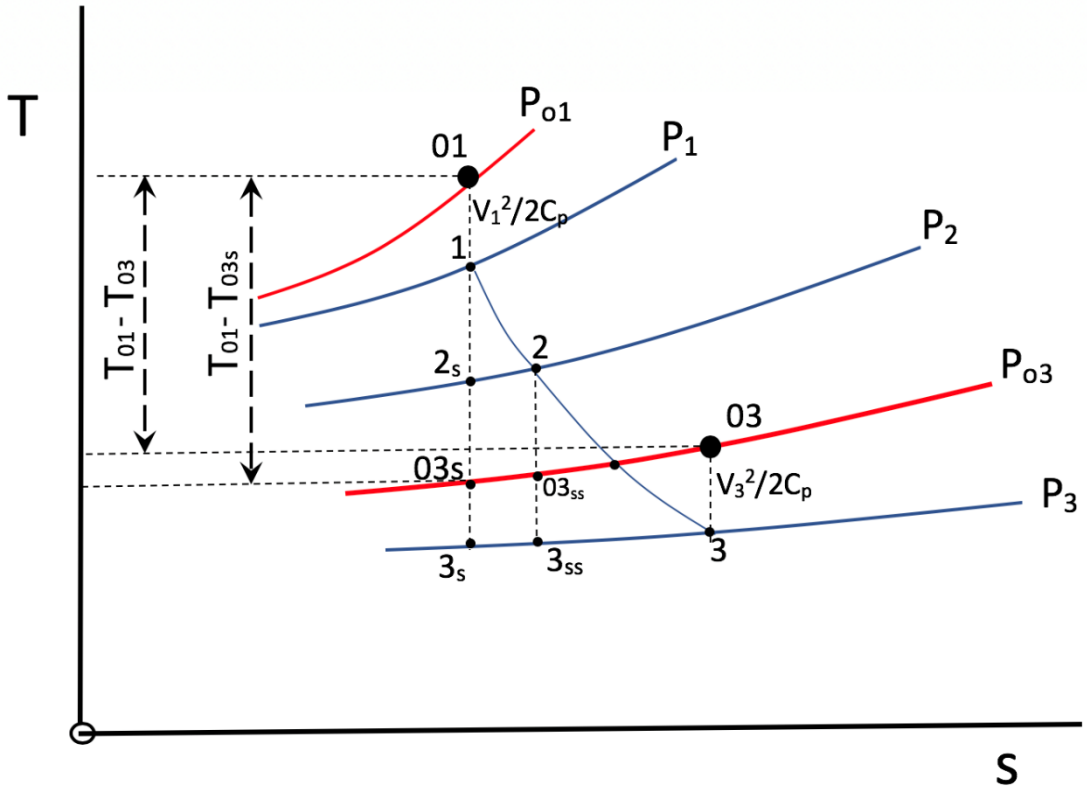

Figure 5-6 Temperature v/s entropy chart

$$\eta_{TT} = \frac{h_{01}-h_{03}}{h_{01}-h_{03s}} = \frac{1-\frac{T_{03}}{T_{01}}}{1-\left(\frac{P_{03}}{P_{01}}\right)^{\frac{\gamma-1}{\gamma}}} \qquad (5\text{-}2)$$

Equation (5-2) shows the total-to-total efficiency in terms of enthalpy. From the boundary conditions value of T_{01}=289 K and P_{01}=101360 Pa and using the pressure ratio and temperature ratio from Table 2-1 P_{03} and T_{03} can be computed. Using equation 5-4 and 5-5, $\partial\eta_{TT}/\partial T_{03}$ and $\partial\eta_{TT}/\partial P_{03}$ can be computed. Assuming the error in temperature

measurement δT_{03} varies from 0 to 2K and error in pressure measurement δP_{03} varies from 0 to 100 Pa.

$$\delta\eta_{TT} = \sqrt{\left[\frac{\partial\eta_{TT}}{\partial T_{03}}\delta T_{03}\right]^2 + \left[\frac{\partial\eta_{TT}}{\partial P_{03}}\delta P_{03}\right]^2} \qquad (5\text{-}3)$$

$$\frac{\partial\eta_{TT}}{\partial T_{03}} = -\frac{1}{T_{01}.\left[1-\left(\frac{P_{03}}{P_{01}}\right)^{\frac{\gamma-1}{\gamma}}\right]} \qquad (5\text{-}4)$$

$$\frac{\partial\eta_{TT}}{\partial P_{03}} = \frac{\frac{\gamma-1}{\gamma}.\left(\frac{P_{03}}{P_{01}}\right)^{\frac{-1}{\gamma}}.\left(1-\frac{T_{03}}{T_{01}}\right)}{\left[1-\left(\frac{P_{03}}{P_{01}}\right)^{\frac{\gamma-1}{\gamma}}\right]^2} \qquad (5\text{-}5)$$

This chapter discussed the total-to-total efficiency of the AFTRF stage. A minute change (0.6 K) in the stage total temperature ratio had a significant effect on the efficiency plot. A case study was performed numerically to determine the effect of the stage total temperature ratio on the LP (AFTRF) and HP turbines.

.

Chapter 6 **Conclusions and Future Work**

The experimental data were taken from the AFTRF with 23 stationary NGV and 29 HP rotor blades. Computational simulations were conducted using STAR CCM+ (RANS with k-ω SST turbulence model and Gamma transition model). The blade loading at the midspan of the NGV and rotor were shown for a grid dependency study. 3.0 million cells were used in an unstructured mesh for each NGV and rotor blade case. Computational data was collected at the same measuring plane location as the experimental data. For the NGV validation, the NGV exit static pressure coefficient and the total pressure coefficient, along with three velocity components at x/c=1.025 were compared. For the rotor validation, the total pressure coefficient at the inlet plane and the three velocity components at the rotor exit were compared. After validating the NGV and the rotor, the stage total pressure ratio and the stage total temperature ratio were also compared to the experimental data. The stage inlet location was one chord upstream of the NGV and the stage outlet location was x/c=1.5 downstream of the rotor's trailing edge. Computational data were in accordance with the experimental data. The deviation in the computational data could be attributed to the following:

1. The rim seal (the wheelspace cavity) flow near the hub was simplified as a wall in the computation.

2. The slot created in the experimental facility to traverse the probes to get the measurements in the rotating frame of reference might have allowed leakage near the casing.

After validating the NGV and the rotor, the total-to-total efficiency was computed. Total-to-total efficiency was based on the stage total pressure ratio and the stage total temperature ratio. A slight increase in the stage total temperature (0.6 K) changed the efficiency by 10%. A case study was also presented to determine the effect of stage temperature ratio on LP and HP turbines. For LP turbines changing the exit total temperature by 0.6 K changed the efficiency by 10% whereas for HP turbine the change in efficiency was 1%.

Future work

This computational validation has shown that the experimental nature of the AFTRF can be accurately modeled computationally. Future work should study the model in the frequency domain instead of in the periodic surface domain. Unsteady analysis would also assist in understanding the time-dependent effects on the flow physics. Different tip designs could be simulated without running expensive experiments. Tip clearance could also be changed in the computational models, and the results could be studied to understand tip-leakage physics in more detail with the help of streamline animations in CFD.

APPENDIX AFTRF model and Solid Geometry Measurements

Scanned model of NGV and Rotor.

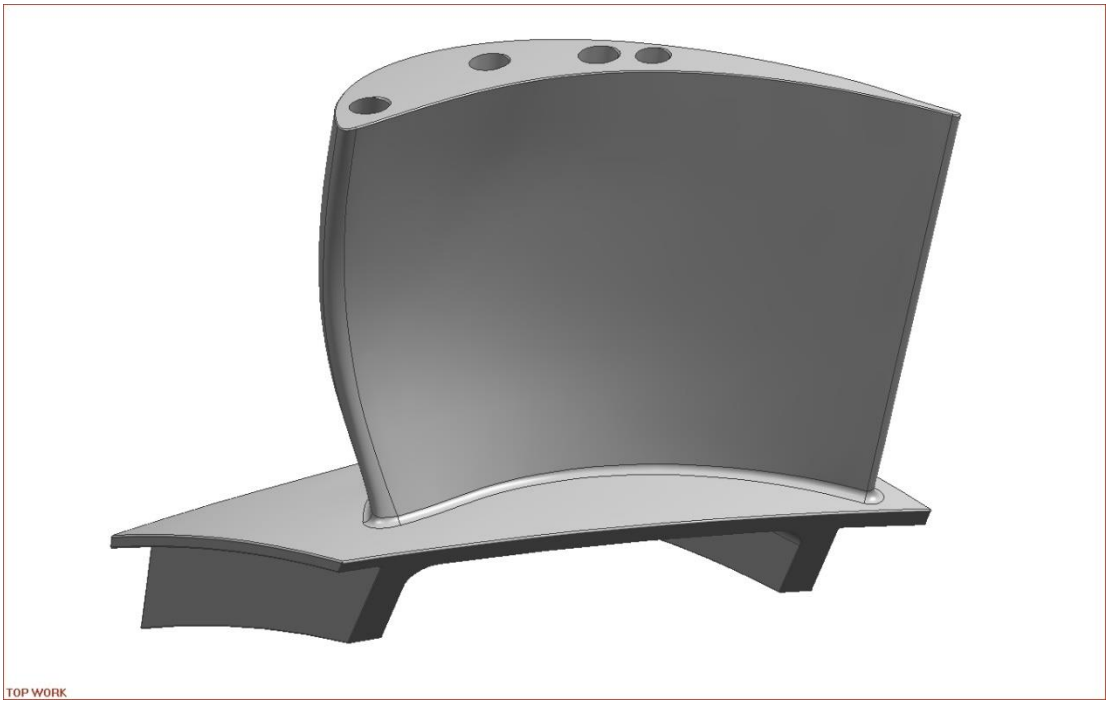

Figure A-1 NGV scanned image-1

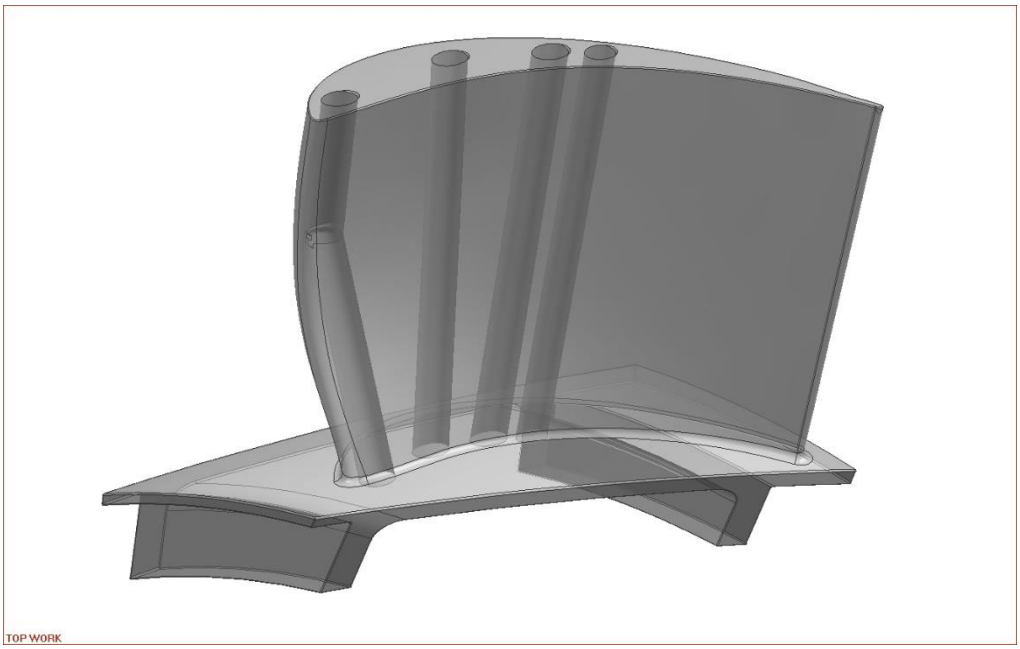

Figure A-2 NGV scanned imgae-2

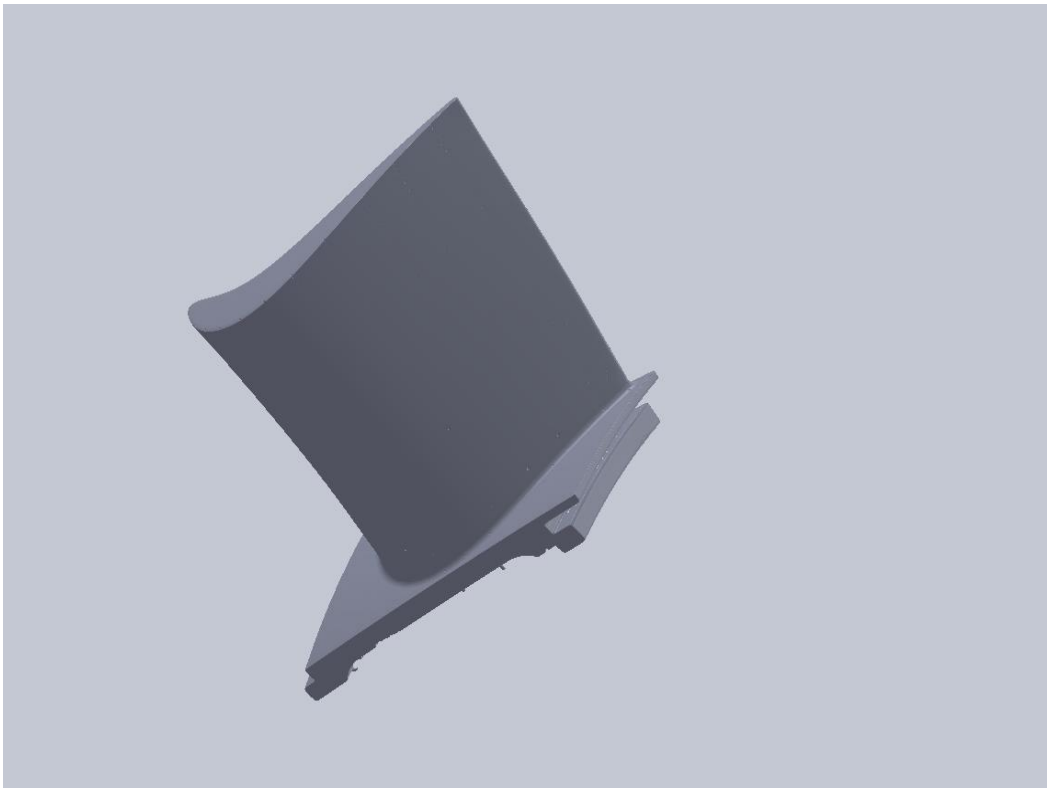

Figure A-3 Rotor scanned image-1

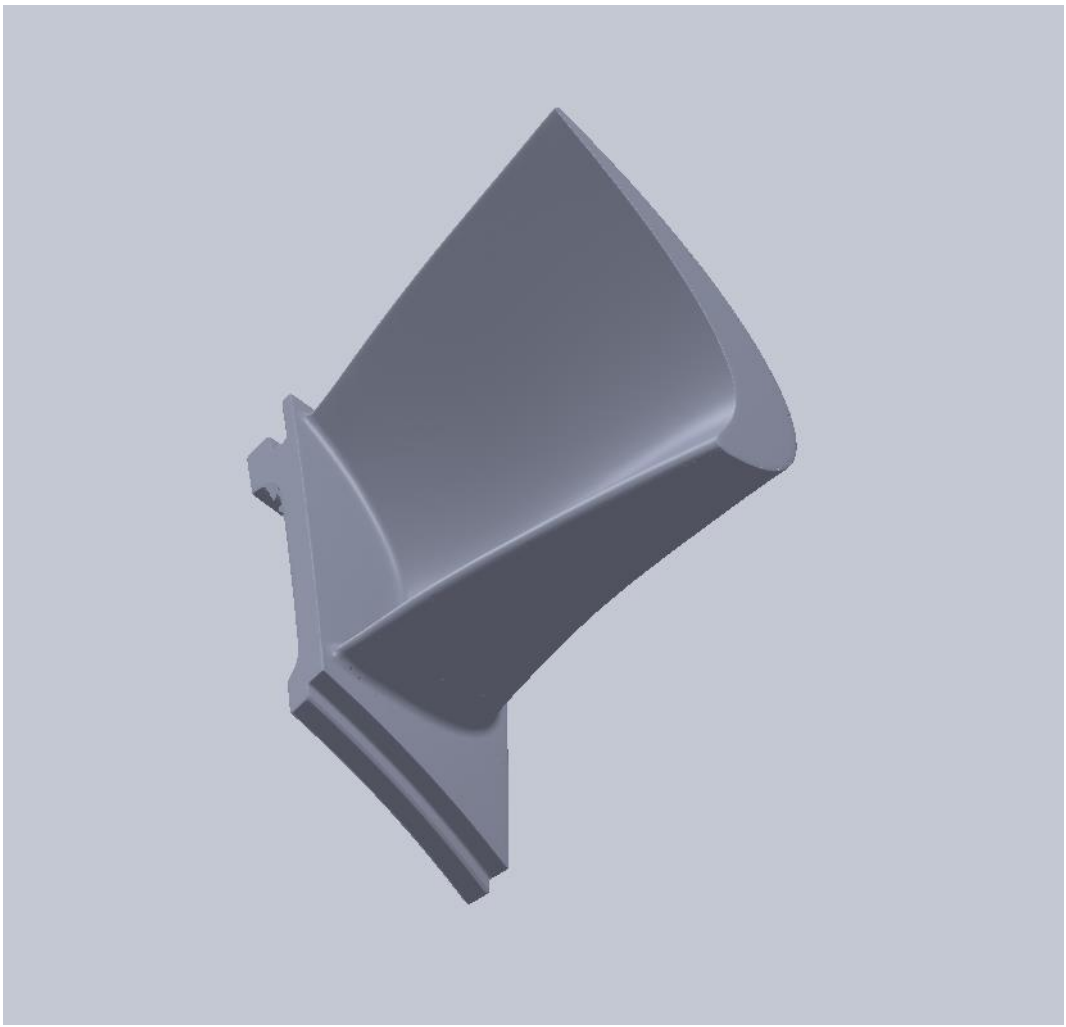

Figure A-4 Rotor scanned image-2

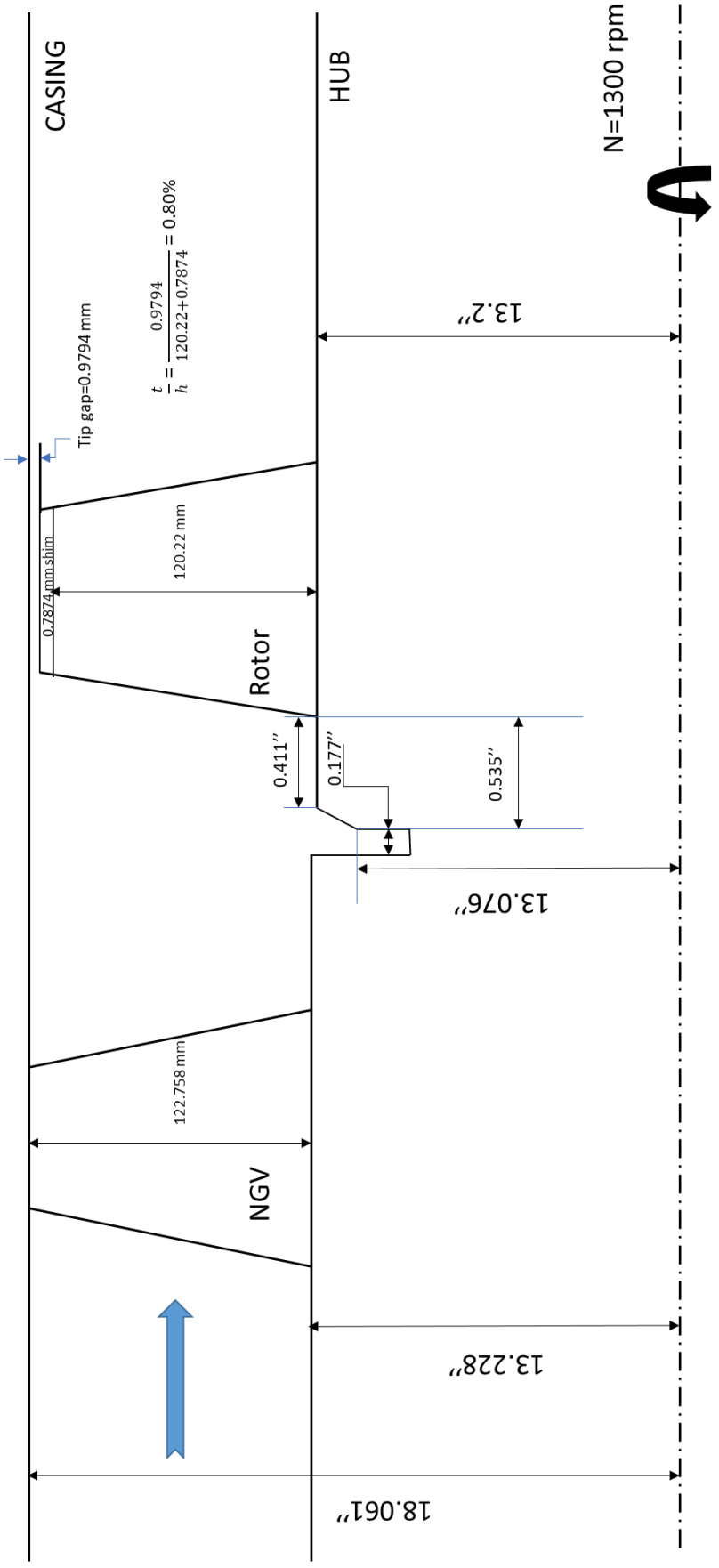

Figure A-5 AFTRF schematic including ngv and rotor

References

[1] http://www.moparmax.com/features/2013/viii_2-turbine/Jet_engine.jpg

[2] Lewis, R.I, "Turbomachinery Performance Analysis", Butterworth-Heinemann, 1996.

[3] Sieverding, C. H. 1985, "Recent Progress in the Understanding of Basic Aspects of Secondary Flows in Turbine Blade Passages." ASME. *J. Eng. Gas Turbines Power*. 107(2):248-257. doi:10.1115/1.3239704.

[4] Langston, L. 2001, "Secondary Flows in Axial Turbines—A Review." Annals of the New York Academy of Sciences, 934: 11-26. doi: 10.1111/j.1749-6632.2001.tb05839.x

[5] Bunker, R.S., 2006 "Axial Turbine Blade Tips: Function, Design, and Durability." Journal of Propulsion and Power, Vol. 22, No. 2, pp. 271-285.

[6] Goldstein, R.J., Spores R.A., 1988 "Turbulent Transport on the Endwall in the Region between Adjacent Turbine Blades." ASME. *J. Heat Transfer* 110(4a):862-869. doi:10.1115/1.3250586.

[7] Sharma, O. P., Butler, T.L., 1986 "Predictions of Endwall Losses and Secondary Flows in Axial Flow Turbine Cascades." ASME. Turbo Expo: Power for Land, Sea, and Air, *Volume 1: Turbomachinery* ():V001T01A098. doi:10.1115/86-GT-228.

[8] Sonoda, T., 1985 "Experimental Investigation on Spatial Development of Streamwise Vortices in a Turbine Inlet Guide Vane Cascade." ASME. Turbo Expo: Power for Land, Sea, and Air, *Volume 1: Aircraft Engine; Marine; Turbomachinery; Microturbines and Small Turbomachinery* ():V001T03A010. doi:10.1115/85-GT-20.

[9] Dey, D., 2001 “Aerodynamic Tip Desensitization in Axial Flow Turbines” PhD dissertation, The Pennsylvania State University, PA

[10] Lakshminarayana, B., Horlock, J.H., 1963 “Review: Secondary flows and losses in Cascades and Axial flow turbomachines.” International Journal of Mechanical Sciences, ISSN: 0020-7403, Vol: 5, Issue: 3, Page: 287-307

[11] Sjolander, S. A., 1997, “Overview of Tip-Clearance Effects in Axial Turbines,” Secondary and Tip Clearance Flows in Axial Turbines VKI Lecture Series 1997-01, Von Karman Institute for Fluid Dynamics, Rhode-St-Genèse, Belgium

[12] Camci, C., 2004 “Turbine Research Facility to Study Tip Desensitization Including Cooling Flows” VKI Lecture series.

[13] Zaccaria, M.A. (1994) “An Experimental Investigation into the Steady and Unsteady Flow Field in An Axial Flow Turbine,” Ph.D. dissertation, The Pennsylvania State University, PA

[14] Turgut, O. H., Camcı, C., 2012 “Computational Validation of the Flow through a Turbine Stage and the Effects of Rim Seal Cavity Leakage on Secondary Flows.” ASME. Turbo Expo: Power for Land, Sea, and Air, *Volume 8: Turbomachinery, Parts A, B, and C* ():1459-1472. doi: 10.1115/GT2012-69306.

[15] Town, J., 2015 **“**A Time Efficient Adaptive Gridding Approach and Improved Calibrations in Five_Hole Probe Measurements." Special Issue on, "Advances in Measurement Techniques for Turbomachinery Flow, Heat Transfer, and Acoustics (AMTT)" by IJRM International Journal of Rotating Machinery, 376967.

[16] Menter, F.R., 1994 “Two equation eddy viscosity turbulence models for engineering applications” AIAA Journal 32:8, 1598-1605

[17] STAR CCM+ 12.04.010-R8 User Manual.

http://www.cd-adapco.com/products/star-ccm/documentation

[18] Peric, M., 2004 “Flow Simulation using control volumes of arbitrary polyhedral shape” ERCOFTAC Bulletin.